



Calhoun: The NPS Institutional Archive
DSpace Repository

Theses and Dissertations

1. Thesis and Dissertation Collection, all items

1994-03

X-ray diffraction studies of evaporated gold thin films deposited on aluminum nitride substrates

Munns, Clifford B.

Monterey, California. Naval Postgraduate School

<http://hdl.handle.net/10945/28654>

Downloaded from NPS Archive: Calhoun



<http://www.nps.edu/library>

Calhoun is the Naval Postgraduate School's public access digital repository for research materials and institutional publications created by the NPS community. Calhoun is named for Professor of Mathematics Guy K. Calhoun, NPS's first appointed -- and published -- scholarly author.

Dudley Knox Library / Naval Postgraduate School
411 Dyer Road / 1 University Circle
Monterey, California USA 93943

DUDLEY KNOX LIBRARY
NAVAL POSTGRADUATE SCHOOL
MONTEREY CA 93943-5101

Approved for public release; distribution is unlimited.

X-Ray Diffraction Studies of Evaporated Gold Thin Films
Deposited on Aluminum Nitride Substrates

by

Clifford B. Munns
Lieutenant Commander, United States Navy
B.S., Virginia Military Institute, 1980

Submitted in partial fulfillment
of the requirements for the degree of

MASTER OF SCIENCE IN MECHANICAL ENGINEERING

from the

NAVAL POSTGRADUATE SCHOOL
March 1994

REPORT DOCUMENTATION PAGE			Form Approved OMB No. 0704	
Public reporting burden for this collection of information is estimated to average 1 hour per response, including the time for reviewing instruction, searching existing data sources, gathering and maintaining the data needed, and completing and reviewing the collection of information. Send comments regarding this burden estimate or any other aspect of this collection of information, including suggestions for reducing this burden, to Washington headquarters Services, Directorate for Information Operations and Reports, 1215 Jefferson Davis Highway, Suite 1204, Arlington, VA 22202-4302, and to the Office of Management and Budget, Paperwork Reduction Project (0704-0188) Washington DC 20503.				
1. AGENCY USE ONLY		2. REPORT DATE 24 March 1994		3. REPORT TYPE AND DATES COVERED Master's Thesis
4. TITLE AND SUBTITLE X-RAY DIFFRACTION STUDIES OF EVAPORATED GOLD THIN FILMS DEPOSITED ON ALUMINUM NITRIDE SUBSTRATES			5. FUNDING NUMBERS	
6. AUTHOR(S) <i>Clifford B. Munns</i>				
7. PERFORMING ORGANIZATION NAME(S) AND ADDRESS(ES) Naval Postgraduate School Monterey, CA 93943-5000			8. PERFORMING ORGANIZATION REPORT NUMBER	
9. SPONSORING/MONITORING AGENCY NAME(S) AND ADDRESS(ES) NCCOSC - RDT & E Div CODE 551 271 CATALINA BLVD SAN DIEGO, CA 92110			10. SPONSORING/MONITORING AGENCY REPORT NUMBER	
11. SUPPLEMENTARY NOTES The views expressed in this thesis are those of the author and do not reflect the official policy or position of the Department of Defense or the U.S. Government.				
12a. DISTRIBUTION/AVAILABILITY STATEMENT Approved for public release; distribution is unlimited.			12b. DISTRIBUTION CODE *A	
13. X-ray diffraction was utilized to determine the root mean square (r.m.s.) strains and average particle sizes in evaporated gold thin films on aluminum nitride substrates as a function of substrate surface condition prior to deposition. The substrate treatments evaluated were surface roughness, use of titanium and chromium inter-layers, presence of an oxide layer on the substrate surface and vacuum conditions used during deposition. The Warren-Averbach method was utilized to obtain the r.m.s. strains and particle sizes from peak breadth data, using both cosine and modulus methods. It was concluded that the highest strain deviations and, therefore, the largest film plastic deformation occurred when the substrate surface was rough, when chromium was used as an inter-layer and when ultra high vacuum conditions were used during deposition. It is proposed that for a fixed film-substrate system, the r.m.s. strain, which is indicative of the level of plastic deformation in the film induced due to differential contraction following deposition, may serve as an indirect measure of the interfacial adhesion.				
14. SUBJECT TERMS X-RAY DIFFRACTION, RMS STRAIN, THIN FILMS, ALUMINUM NITRIDE, GOLD, WARREN-AVERBACH			15. NUMBER OF PAGES 71	
			16. PRICE CODE	
17. SECURITY CLASSIFICATION OF REPORT Unclassified	18. SECURITY CLASSIFICATION OF THIS PAGE Unclassified	19. SECURITY CLASSIFICATION OF ABSTRACT Unclassified	20. LIMITATION OF ABSTRACT UN	

ABSTRACT

X-ray diffraction was utilized to determine the root mean square (r.m.s.) strains and average particle sizes in evaporated gold thin films on aluminum nitride substrates as a function of substrate surface condition prior to deposition. The substrate treatments evaluated were surface roughness, use of titanium and chromium inter-layers, presence of an oxide layer on the substrate surface and vacuum conditions used during deposition. The Warren-Averbach method was utilized to obtain the r.m.s. strains and particle sizes from peak breadth data, using both cosine and modulus methods. It was concluded that the highest strain deviations, and therefore, the largest film plastic deformation, occurred when the substrate surface was rough, when chromium was used as an inter-layer and when ultra high vacuum conditions were used during deposition. It is proposed that for a fixed film-substrate system, the r.m.s. strain, which is indicative of the level of plastic deformation in the film due to differential contraction following deposition, may serve as an indirect measure of the interfacial adhesion.

110515
M/35115
C.1

TABLE OF CONTENTS

I.	INTRODUCTION.....	1
II.	BACKGROUND.....	5
	A. ALUMINUM NITRIDE.....	5
	1. Microstructure.....	5
	2. Fabrication.....	5
	3. Metallization.....	7
	B. STRAIN/CRYSTALLITE SIZE MEASUREMENTS BY X-RAY DIFFRACTION: SUMMARY OF THE WARREN-AVERBACH METHOD.....	11
	1. Representation of a Periodic Function by a Fourier Series.....	11
	2. The Measured, Instrumental and Diffraction Profiles.....	14
	3. The Fourier Transform or Stokes Deconvolution.....	16
	4. Determination of Lattice Strains and Crystallite Size.....	19
	C. PHYSICAL SIGNIFICANCE OF THE RESULTS OBTAINED FROM THE WARREN-AVERBACH ANALYSIS.....	28
III.	EXPERIMENTAL.....	32
	A. MATERIALS.....	32
	B. EQUIPMENT.....	32
	1. Evaporator Chamber and Sub Components.....	32

2. Film Thickness Monitor..... 34

C. PROCEDURE..... 37

1. Gold Standard Preparation..... 37

2. Substrate Surface Preparation.....37

3. Metallization Procedure.....38

D. XRD PROCEDURES.....40

1. Parameters For XRD Scanning..... 40

2. Post XRD Scan Process..... 40

IV. RESULTS AND DISCUSSION..... 47

A. RESULTS SUMMARY..... 47

1. R.M.S. Strain, Particle Size and Stress Deviation.....47

2. Discussion.....47

3. Uncertainty..... 52

V. CONCLUSIONS.....54

VI. RECOMMENDATIONS.....56

LIST OF REFERENCES..... 57

INITAL DISTRIBUTION LIST.....62

LIST OF TABLES

TABLE 1. PROPERTIES OF ALN AND OTHER CERAMIC SUBSTRATES.... 4

TABLE 2. SUMMARY OF SURFACE TREATMENTS..... 37

TABLE 3. RESULTS SUMMARY.....48

TABLE 4. UNCERTAINTY SUMMARY..... 53

LIST OF FIGURES

Figure 1.	Chip Power Dissipation Versus Time.....	4
Figure 2.	Lattice Structure for AlN.....	6
Figure 3.	Representation of a Periodic Function.....	12
Figure 4.	Graphical Representation of a Deconvoluted Profile.....	15
Figure 5.	Real Space Representation of a Columnar Material Used in the Warren-Averbach Derivation.....	22
Figure 6.	Reciprocal Space Representation of a 00 l Reflecting Plane Used in the Warren-Averbach Derivation.....	22
Figure 7.	Plot of $\ln A_n^s(l)$ versus l^2	27
Figure 8.	Plot of A_n^s versus n	27
Figure 9.	Plot of A_L^s versus L	27
Figure 10.	Chamber Layout and Equipment Block Diagram.....	33
Figure 11.	Calculation of the Tooling Factor From Metallization Geometry.....	36
Figure 12.	XRD Scan of Gold.....	43
Figure 13.	XRD Scan of AlN.....	44
Figure 14.	Separation of the Au (111) Peaks.....	45
Figure 15.	Separation of the Au (222) Peaks.....	46

ACKNOWLEDGMENTS

Partial funding of this thesis work was provided by NCCOSC, RDT&E Division, San Diego, Ca. The contributions to this project by Mr. Pat Sullivan, project monitor, is gratefully acknowledged.

I. INTRODUCTION

Since the electronic revolution of the 1960's and 70's, the electronics industry has striven for ever smaller and ever more powerful electronic circuits. Figure 1 charts the evolution of circuit power dissipation requirements over time. The steadily increasing demand on small circuit size, cost and reliability results in the constant search for improved heat dissipation designs. Since an integrated circuit must typically be maintained below 80 to 100°C for component reliability, and is usually subjected to numerous thermal cycles during its lifetime, proper design of packages for modern electronic components pose some serious challenges.

One of the principal properties of concern is the thermal conductivity of the substrate on which chips are mounted. A higher thermal conductivity allows for increased heat removal capability and a higher circuit density. Aluminum nitride (AlN) offers an attractive choice for chip substrates over other substrates such as alumina (Al_2O_3) and beryllium oxide (BeO). Table 1 lists engineering properties of importance of materials currently used as chip substrates and how they compare to AlN. Although Table 1 lists the thermal conductivity of AlN as ranging from 100-170 W/K-m, it has a theoretical value of over 300 W/K-m and other attractive properties such as cost, ease of manufacture, non toxicity and good insulating capacity [Ref. 3, 4], which make it very attractive as a substrate material for ceramic packages.

Metallization (the placement of a thin conductive metal film on the substrate surface) is a vital step in providing interconnects between devices, and for the attachment of seal

rings to the substrate. The metal film, which may be applied to the substrate by thin film processes (such as vacuum evaporation or sputtering) must adhere to the substrate under the presence of thermal stresses caused by thermal cycling without cracking or peeling.

Recent attempts to improve copper and gold film adhesion to AlN substrates have been successful, but involve application of oxide layers or use of metal pastes that typically lower the overall thermal conductivity of the product. Gold, being inert and possessing good conductive properties, is a commonly used metallization, however, little information is available on the influence of various process parameters on the adhesion of gold films to AlN substrates. Especially little systematic information is available on the impact of substrate surface conditions prior to metallization on adhesion and the state of stress of the film.

Since X-ray diffraction (XRD) is completely nondestructive, it has been used extensively to study strains and/or stresses in crystalline thin films through the study of diffraction peak shifts and peak broadening. While techniques based on peak shifts yield the average long-range strains/stresses in materials [Ref. 5], those based on peak breadths yield a measure of strain/stress dispersion (i.e., the deviation of the strains/stresses from the mean long-range value). Of the techniques based on line breadth, the Fourier method of Warren and Averbach [Ref. 6] is best characterized mathematically, and yields a measure of both the average crystallite size (which may represent grain/subgrain size or inter-dislocation spacing) and the root mean square (r.m.s.) strain, which represents local variations of the lattice strain from the mean long range strain value. Since these deviations usually occur due to plastic deformation, the strain dispersion can be used as a measure of the degree of plastic deformation of the films due to differential thermal contraction of the film and the substrate during cooling following deposition. Further, for a given pair of film and substrate materials, better interfacially bonded systems are

expected to undergo a larger degree of plastic deformation, therefore, strain dispersions obtained from peak breadths may serve as an indirect measure of interfacial adhesion.

Accordingly, the goal of this study has been to use the Warren and Averbach technique to determine crystallite size and r.m.s. strains following metallization using different process conditions (primarily, different substrate surface conditions) to qualitatively examine the influence of these conditions on metallization stresses and adhesion.

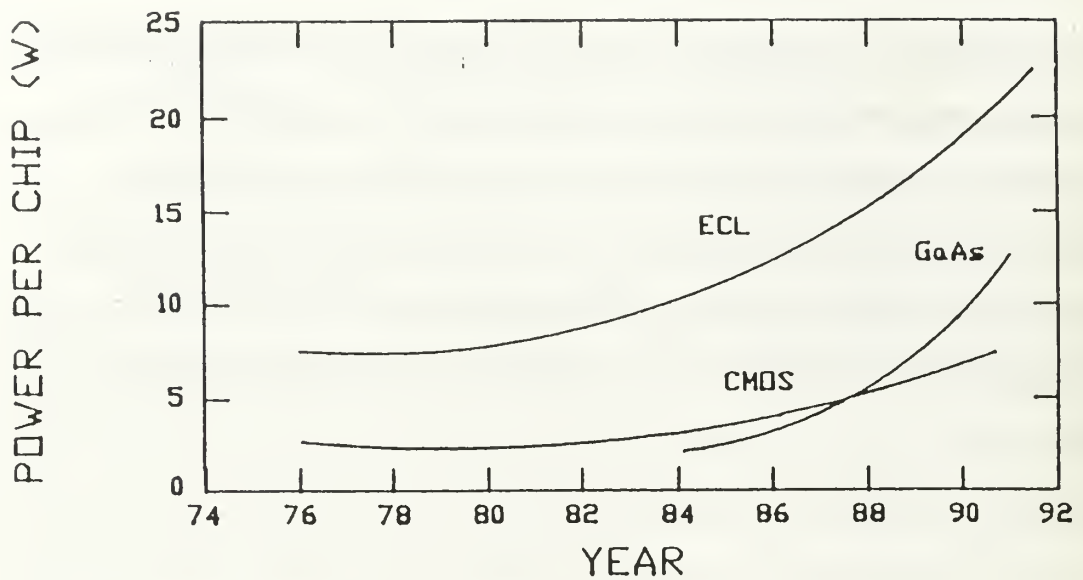


Figure 1. Chip Power Dissipation Over Time [Ref. 1]

Table 1. PROPERTIES OF ALN AND OTHER CERAMIC SUBSTRATES [Ref. 2]

	AlN	Al ₂ O ₃	BeO	SiC
Thermal Cond. (W/m-K)	100-170	20	250	270
Coeff. Th. Exp. ($\times 10^{-6} / ^\circ \text{C}$)	4.5	7.3	8.0	3.7
Dielectric Str. (20°C)(kV/mm)	14-17	10	10-14	0.07
Density (g/cm ³)	3.3	3.9	2.9	3.2
Bend Str. (MPa)	3.9-4.9	2.9	1.6-2.3	4.4
Young Mod. ($\times 10^7$)(MPa)	2.81	3.7	3.2	4.0
Sintering Temp. (°C)	1800	1500		2000

II. BACKGROUND

A. ALUMINUM NITRIDE

1. Microstructure

The ceramic, Aluminum Nitride (AlN) is a covalent compound formed by the reaction of aluminum and nitrogen. After formation, AlN crystallizes in a hexagonal wurtzite structure as shown in Figure 2. AlN possesses a closed packed AlN double layer and is not known to form polytypes, wherein the lattice takes on a cubic structure [Ref. 8]. The microstructure can be severely altered in the presence of oxygen whereby the oxygen replaces three nitrogen atoms at the exclusion of one aluminum atom [Ref. 9]. The effect of oxygen on the lattice structure is of importance when considering metallization treatments and the thermal properties of AlN and is addressed later. General properties of AlN are given in Table 1.

2. Fabrication

There are several techniques available to form AlN powder allowing for great flexibility. Additionally, the raw materials needed to produce AlN powder are abundant and relatively inexpensive. The most common ways to commercially make AlN powder is by the reaction of ammonia with aluminum chloride or by direct nitration of metallic aluminum followed by carbon reduction in a nitrogen environment [Ref. 10]. More recent methods include chemical vapor deposition, polymer pyrolysis and arc plasma techniques [Ref. 11, 12].

A critical requirement in the production of useful AlN powder is the purity level achieved during production. Excessive amounts of carbon or oxygen contaminants can reduce the thermal conductivity of AlN product following sintering. Additionally, the

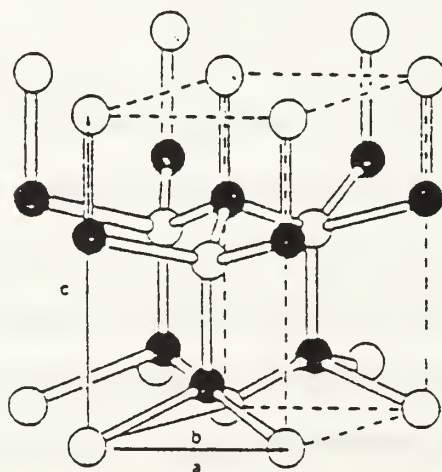
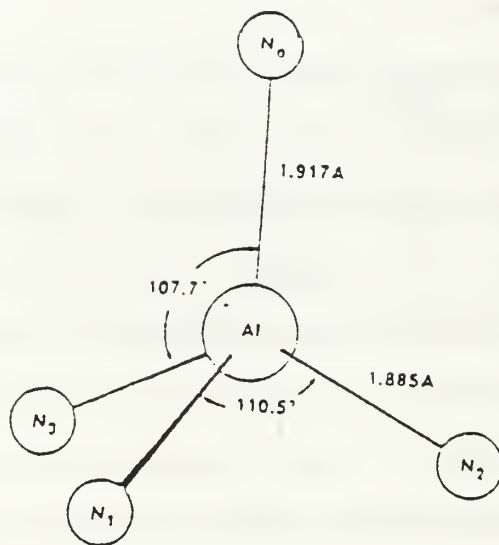


Figure 2. Lattice Structure for AlN [Ref. 7]

presence of contaminants can hinder the adhesion of metal thin films to the substrate surface. The latest techniques currently in use have resulted in AlN powder oxygen levels as low as 1% and carbon levels as low as 0.02 weight percent [Ref. 13, 14].

The method chosen to manufacture the AlN powder also affects the resulting particle size, a key parameter in the sintering process. Current techniques offer a range of grain sizes from as small as 30 nm up to 8 microns [Ref. 15].

Following powder production, sintering is required to form the final product. Several sintering aids have recently been studied with varying effectiveness. The most common sintering aids include rare-earth or alkaline-earth oxides, such as calcium oxide, yttrium fluoride, calcium fluoride and yttria [Ref. 16, 17]. Additionally, carbon doping is often performed during the sintering operation [Ref. 18]. The choice of sintering aids and doping agents have a significant impact on oxygen diffusion, final particle size, densification and thermal conductivity [Ref. 19]. Some recent methods have resulted in a densification as high as 99% of theoretical and a thermal conductivity as high as 260 W/K-m, a nearly ten fold increase when compared to the thermal conductivity of alumina [Ref. 20, 21].

3. Metallization

Metallization of AlN substrates is not a perfected procedure and is under current study by a variety of institutions and companies. While some successes have been achieved in improving the adhesive strength of metal thin films to the substrate surface, this often results in a reduction in thermal conductivity. Processes currently under study are now briefly examined.

Co-firing AlN with tungsten and with Mo-Mn using fritted pastes has resulted in good adhesion strengths, relying on metal diffusion and subsequent mechanical interlocking [Ref. 22]. Normal adhesion strengths greater than 20 MPa have been

reported using this method, but due to the low electrical conductivity of W and Mo, resistive heating effects have reduced the thermal conductivity by 19% and 9% respectively [Ref. 23,24].

Thick film metallization of AlN substrates, using commercially available pastes of Au, Cu and Ag-Pd, has similarly proven to be successful, resulting in normal adhesion strengths from about 14 MPa to 18 MPa, but is limited by the formation of either a glassy phase or a mixed oxide layer near the interface that results in an insulating effect [Ref. 25-29].

Due to the absence of a glassy phase, which could otherwise be exploited for bonding, metallization using fritted pastes of various metallic oxides and glassy pastes, have been performed resulting in normal adhesive strengths as high as 20MPa. However, problems encountered with these methods include the need for exceptionally pure pastes, chemical and thermomechanical incompatibility between the paste and substrate, oxygen diffusion, and the formation of a glassy inter-layer which causes an insulating effect [Ref. 30]. Improper control of the paste chemistry can result in poor adhesion, and presence of a glassy inter-layer has limited the achieved thermal conductivity to about 150 W/K-m using these methods [Ref. 31].

Directly bonded copper (DBC) metallizations, which rely on Cu-O bonding, have been successfully applied to AlN substrates yielding peel strengths as high as 8.5 kg/cm [Ref. 32]. The success of the DBC method was found to be strongly dependent on the thickness of a pre-applied oxide layer that promotes Cu-O bonding, but lowers the thermal conductivity of the finished product due to the formation of Al_2O_3 and Cu_2O , both of which have a thermal conductivity lower than that of AlN [Ref. 33].

Oxygen diffusion can be a problem when processing AlN for metallization, even at near ambient temperatures, since the surface of the substrate can quickly pick up

oxygen from the air forming Al_2O_3 at the interface in a matter of hours [Ref. 34].

Impurity pickup, especially carbon pickup, is also a handling concern. Methods to reduce hydrocarbons at the substrate surface, therefore, is an important processing requirement.

With respect to the methods of metallization outlined above, metallization of AlN with highly conductive films, such as Au or Cu, appear to hold promise in both providing good electrical conductivity as well as avoiding a reduction in the thermal conductivity, if they can be reliably adhered to the substrate surface.

Substrate surface roughness is likely to influence mechanical interlocking at the interface, hence, the adhesion of thin films to substrates. However, no systematic study of the effect of substrate surface finish on stress and adhesion in films on AlN has been reported to date. Therefore, substrate surface roughness was a chosen variable in this study. Unoxidized AlN substrates of varying surface roughness metallized with pure gold were examined using XRD.

Studies of the metal-AlN interface have shown that the interfacial bond is controlled by a metal-AlN interaction vice a metal-O interaction in Al_2O_3 metallizations [Ref. 35]. The metal-AlN interaction, and thus the interfacial adhesion, can often be strengthened by depositing a thin inter-layer of a reactive metal (e.g., Ti) between the metallization and the AlN substrate [Ref. 36-38]. Ti has shown to enhance wetting at metal-AlN interfaces via formation of TiN and metallic aluminum. Because of these advantages, the TiN system has been the focus of most studies of thin film metallization to date, yet little quantitative data on the effect of Ti on the strength of metal-AlN interfaces is available. Large residual stresses have been known to be present in thin metal films on ceramic substrates for a long time (with resultant implications on the mechanical properties and the reliability of the interface) [Ref. 39], however, no systematic study of

the dependence of interfacial adhesion on the stresses at thin film/AlN interfaces has been reported.

In addition to a Ti inter-layer, a Cr inter-layer will be investigated. Unlike Ti, Cr does not form any intermetallics with Au yet, Cr forms a solid solution with Al and several Cr_mAl_n -type intermetallics when AlN and Cr are heated to 1000°C [Ref. 40, 41]. This can potentially give rise to good bonding between Cr and AlN, due to the absence of intermetallics in the Au-Cr system, and may yield a metallization-substrate interface with better interfacial mechanical properties than the AlN-Ti system. Therefore, AlN substrates metallized with Au, using Cr and Ti as inter-layers, are investigated in this study.

As outlined above, formation of an oxide layer has been shown to improve bonding in Cu thin films applied to AlN substrates through Cu-O bonding. It is known that Au forms a metal oxide, Au_3O_2 , at temperatures above 500°C [Ref. 42]. However, the effect of the presence of a thin layer of Al_2O_3 on the AlN surface on bonding with Au metallization is not known, and is investigated here.

Thin film metallizations are usually deposited on substrates with ultra high vacuum (UHV) or high vacuum (HV) conditions. Generally, higher vacuum promotes better epitaxial (oriented) crystal growth with the vacuum playing a key role in the thin film microstructure [Ref. 43]. Presently, little information on the effect of metallization pressure on the film characteristics when directly applying Au to AlN substrates is available. Therefore, metallizations under UHV and HV conditions were performed.

Finally, substrate temperature during metallization is also known to profoundly affect epitaxial growth of thin films and may also play a key role in reaction metal bonding at the interface [Ref. 44]. Therefore, metallizations at two different substrate temperatures using unoxidized AlN substrates with Cr inter-layers was performed.

B. STRAIN/CRYSTALLITE SIZE MEASUREMENT BY X-RAY DIFFRACTION: SUMMARY OF THE WARREN-AVERBACH METHOD

1. Representation of a Periodic Function by a Fourier Series

A complete description and derivation of the Warren-Averbach method is available in [Ref. 6, 45, 47]. The summary of the Warren Averbach method presented in the following sections is based on [Ref. 45, 46].

The first step in obtaining quantitative results from X-ray diffraction by the Warren-Averbach method requires representing the diffraction profile by a Fourier series. Since any periodic function can be represented by a Fourier series, one can assume a measured diffraction profile, designated $f(x)$, to be a section of a periodic function having the shape of the measured profile as shown in Figure 3. It can be shown that this function can be represented by

$$f(x) = \sum_{n=-\infty}^{+\infty} \left[A_n \cos 2\pi n \left(\frac{x}{a} \right) + B_n \sin 2\pi n \left(\frac{x}{a} \right) \right] \quad (1)$$

where a is the period of the function, $-\frac{a}{2}$ to $\frac{a}{2}$ is the interval of interest and n takes on integer values and is referred to as the harmonic number. It can also be shown that the Fourier coefficients A_n and B_n , can be solved for by

$$A_n = \frac{1}{a} \int_{-\frac{a}{2}}^{+\frac{a}{2}} f(x) \cos 2\pi n \left(\frac{x}{a} \right) dx \quad (2)$$

$$B_n = \frac{1}{a} \int_{-\frac{a}{2}}^{+\frac{a}{2}} f(x) \sin 2\pi n \left(\frac{x}{a} \right) dx. \quad (3)$$

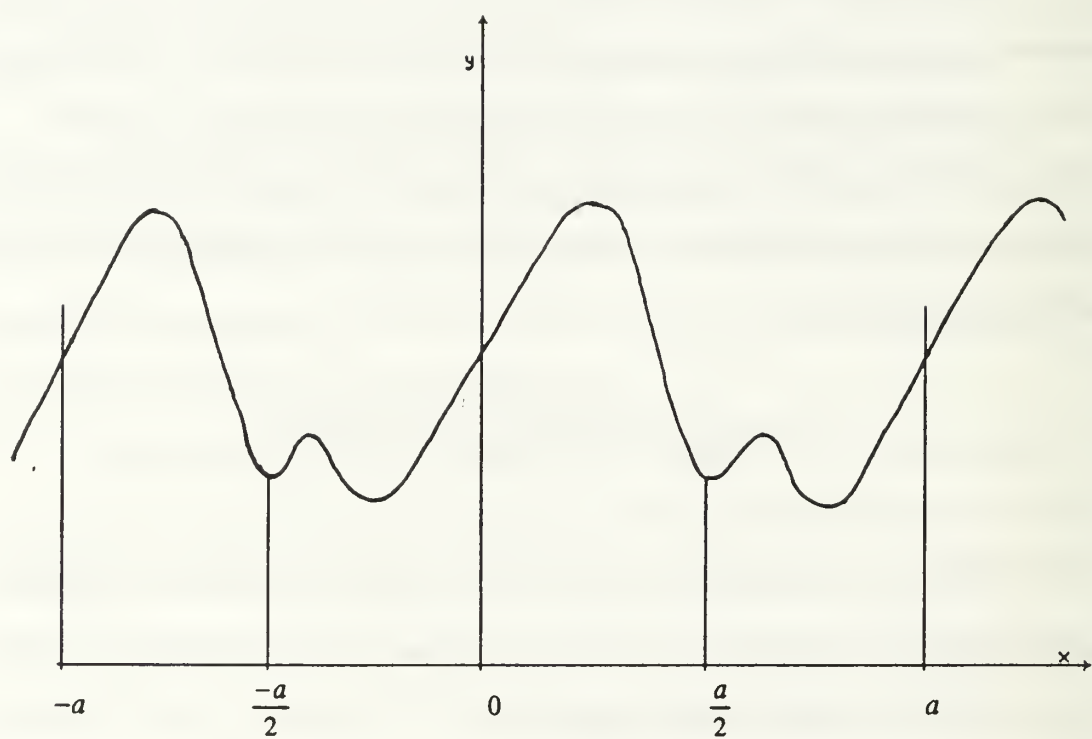


Figure 3. Representation of a Periodic Function [Ref. 47]

Alternatively, equation (1) can be expressed in its complex form as

$$f(x) = \sum_{n=-\infty}^{+\infty} C(n) e^{-2\pi n i(x/a)} \quad (4)$$

where the complex coefficients, C_n , are composed of a real and an imaginary part such that

$$C(n) = C_r(n) + iC_i(n)$$

where the subscript r refers to the real part, and the subscript i refers to the imaginary part.

Since the term $e^{-2\pi n i(x/a)}$ in equation (4) can be expressed in its trigonometric form as

$$e^{-2\pi n i\left(\frac{x}{a}\right)} = \cos 2\pi n \left(\frac{x}{a}\right) - i \sin 2\pi n \left(\frac{x}{a}\right),$$

then

$$f(x) = \sum_{n=-\infty}^{+\infty} \left[C_r(n) \cos 2\pi n \left(\frac{x}{a}\right) + C_i(n) \sin 2\pi n \left(\frac{x}{a}\right) + iC_i(n) \cos 2\pi n \left(\frac{x}{a}\right) - iC_r(n) \sin 2\pi n \left(\frac{x}{a}\right) \right]. \quad (5)$$

In equation (5), the imaginary terms must cancel since $f(x)$ is real. This can only happen if $C(-n) = C^*(n)$, where $C^*(n)$ represents the complex conjugate of $C(n)$. This result allows $C_r(n)$ and $C_i(n)$ to be expressed as

$$C_r(n) = \frac{1}{a} \int_{-\frac{a}{2}}^{+\frac{a}{2}} f(x) \cos 2\pi n \left(\frac{x}{a}\right) dx \quad (6)$$

and

$$C_i(n) = \frac{1}{a} \int_{-\frac{a}{2}}^{+\frac{a}{2}} f(x) \sin 2\pi n \left(\frac{x}{a} \right) dx. \quad (7)$$

Comparing equations (6) and (7) with equations (2) and (3), it is evident that

$$C_r(n) = A_n \quad \text{and} \quad C_i(n) = B_n$$

where $C_r(n)$ represents the real Fourier coefficients and $C_i(n)$ represents the complex Fourier coefficients. Thus, a measured diffraction profile is can be expressed by a Fourier series with real and complex coefficients.

2. The Measured, Instrumental and Diffraction Profiles

The measured peak profile, designated $h(x)$, comprises the instrumental profile in conjunction with the true diffraction profile. The instrumental broadening effect is caused by incident radiation that is not truly monochromatic and the fact that the incident radiation is spread across a finite width of the specimen, vice being confined to an infinitely thin line [Ref. 48]. This instrumental effect is apparent even when the specimen is strain free and of a sufficient particle size that avoids particle size broadening. The measured profile then, is a convolution of the instrumental profile, designated $g(x)$, and the pure profile, designated $f(x)$. Figure 4 represents the situation graphically. Obtaining the instrumental profile, $g(x)$, requires obtaining a diffraction profile of a strain free standard of a sufficiently large particle size, so that neither particle size broadening, nor strain broadening is apparent. The combined effect of $g(x)$ and $f(x)$ can be represented by a convolution integral

$$h(x) = \frac{1}{A} \int_{-\infty}^{\infty} g(z) f(x-z) dz \quad (8)$$

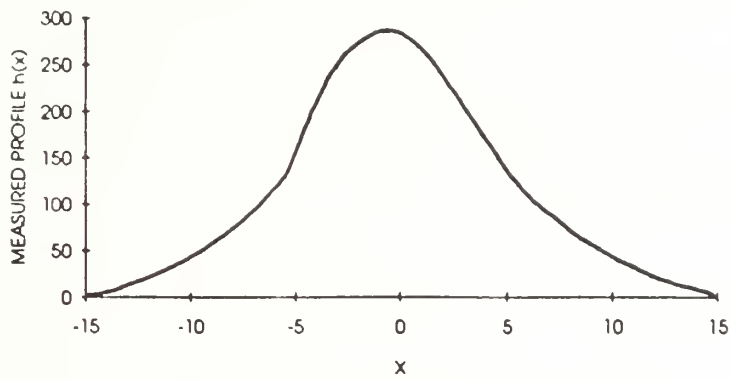


Figure 4.(a) Plot of Measured Profile, $h(x)$

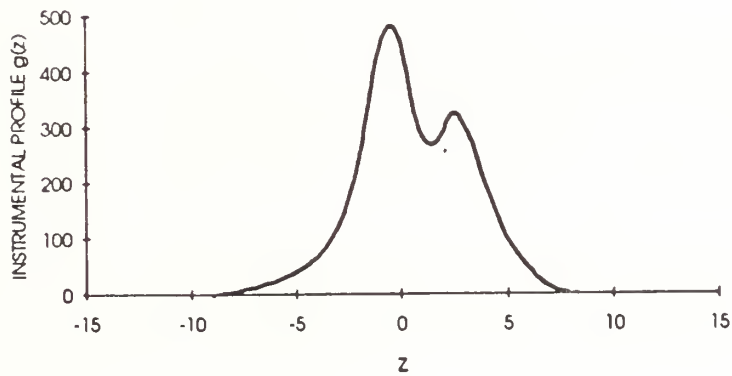


Figure 4.(b) Plot of Instrumental Profile, $g(z)$

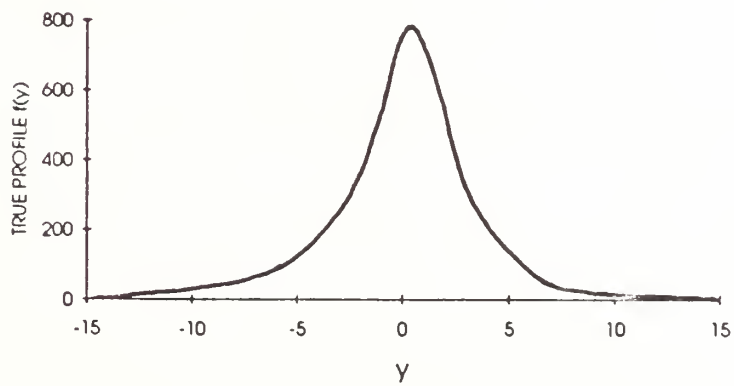


Figure 4.(c) Plot of True Profile, $f(y)$

Figure 4. Graphical Representation of a Deconvoluted Profile [Ref. 49]

where A is the area under the curve $f(y)$.

If convenient shapes (or functions) of the three profiles are assumed (e.g. Cauchy or Gaussian), the relation between the integral line breadths, B , of the three profiles can be expressed as

$$\text{Cauchy: } u = U / (1 + k^2 u^2)$$

$$B^2(h) = B^2(g) + B^2(f)$$

and

$$\text{Gaussian: } u = U e^{k^2 u^2}$$

$$B(h) = B(g) + B(f) \text{ [Ref. 50].}$$

Actual diffraction profiles, however, are neither purely Gaussian nor purely Cauchy, making a Fourier representation of the profiles and subsequent deconvolution necessary.

3. The Fourier Transform or Stokes Deconvolution

Representing $h(x)$, $f(y)$ and $g(z)$ in Fourier series form

$$f(y) = \sum_n F(n) e^{-2\pi n i \left(\frac{y}{a}\right)} \quad (9.1)$$

$$g(z) = \sum_{n'} G(n') e^{-2\pi n' i \left(\frac{z}{a}\right)} \quad (9.2)$$

$$h(x) = \sum_{n''} H(n'') e^{-2\pi n'' i \left(\frac{x}{a}\right)} \quad (9.3)$$

where: F , G and H are the Fourier coefficients and n , n' and n'' are the harmonic numbers. Substituting equations 9.1, 9.2 and 9.3 into equation 8 yields

$$h(x) = \frac{1}{A} \int_{-\infty}^{\infty} \sum_{n'} G(n') e^{-2\pi n' i \left(\frac{z}{a}\right)} \sum_n F(n) e^{-2\pi n i \left(\frac{x-z}{a}\right)} dz$$

where the limits of integration can be replaced by $-\frac{a}{2}$ to $\frac{a}{2}$ so that $g(z)$ is non-vanishing only in this interval. Combining all terms containing z , and replacing the limits of integration yields

$$h(x) = \frac{1}{A} \sum_{n'} \sum_n G(n') F(n) e^{-2\pi n i \left(\frac{x}{a}\right)} \int_{-\frac{a}{2}}^{+\frac{a}{2}} e^{-2\pi i (n' - n) \left(\frac{z}{a}\right)} dz.$$

Since,

$$\int_{-\frac{a}{2}}^{+\frac{a}{2}} e^{-2\pi i (n' - n) \left(\frac{z}{a}\right)} dz = \begin{cases} a & \text{when } n' = n \\ 0 & \text{when } n' \neq n \end{cases}$$

and the condition of interest is $n' = n$, then

$$h(x) = \frac{a}{A} \sum_n G(n) F(n) e^{-2\pi i n \left(\frac{x}{a}\right)} \quad (\text{for } n = 0 \text{ to } \infty). \quad (10)$$

Replacing $h(x)$ in equation (10) by equation (9.3), yields

$$\sum_n H(n) e^{-2\pi n i \left(\frac{x}{a}\right)} = \frac{a}{A} \sum_n G(n) F(n) e^{-2\pi n i \left(\frac{x}{a}\right)}$$

or

$$H(n) = \frac{a}{A} G(n) F(n). \quad (11)$$

Since only profile shape, not profile size, is of interest, the constant $\frac{a}{A}$ can be dropped leaving

$$H(n) = G(n)F(n). \quad (12)$$

This relation can be rewritten in complex form as

$$F_r(n) + iF_i(n) = \frac{H_r(n) + iH_i(n)}{G_r(n) + iG_i(n)}.$$

Multiplying the numerator and denominator by the complex conjugate of $G(n)$ and equating the real and imaginary parts yields

$$F_r(n) = \frac{H_r(n)G_r(n) + H_i(n)G_i(n)}{G_r^2(n) + G_i^2(n)} \quad (13.1)$$

and

$$F_i(n) = \frac{H_i(n)G_r(n) - H_r(n)G_i(n)}{G_r^2(n) + G_i^2(n)}. \quad (13.2)$$

From the two experimentally measured curves $h(x)$ and $g(z)$, the real (cosine) coefficients ($H_r(n)$ and $G_r(n)$) and the imaginary (sine) coefficients ($H_i(n)$ and $G_i(n)$) can be determined. The broadened diffraction profile cosine and sine coefficients are then determined using equations (13.1) and (13.2) allowing the pure diffraction profile to be constructed from

$$f(y) = \sum_n \left[F_r(n) \cos 2\pi n \left(\frac{y}{a} \right) + F_i(n) \sin 2\pi n \left(\frac{y}{a} \right) \right]. \quad (14)$$

4. Determination of Lattice Strains and Crystallite Size

Cold worked metals may contain numerous, non-random dislocation arrays, such as low angle grain boundaries which subdivide the original grains into smaller coherent domains each slightly misoriented from the next. Therefore, non-vanishing diffraction intensities can occur at angles other than that satisfying the exact Bragg condition, resulting in broadening of the diffraction line. Such peak broadening can also occur if the crystal is divided into smaller, relatively misoriented crystallites by random dislocation arrays, or if the crystal particle sizes are very small. Typically, crystallite sizes of 100-1000 Å yield significant diffraction broadening [Ref. 51]. If the broadening is due only to this crystallite size effect, the average crystallite size is given by

$$D_v = \frac{k\lambda}{\beta \cos \theta} \quad (15)$$

where: D_v is the crystallite size in angstroms, k is a proportionality constant close to 1.0,

β is the integral breadth of the true profile such that $\beta = \frac{\text{peak area}}{\text{peak maximum}}$, θ is the Bragg angle and λ is the wavelength of the incident x-rays in Å [Ref. 52]. The dislocations, which produce the subdivisions into domains, can also produce both tensile and compressive strains within each domain. These tensile and compressive strains result in a deviation of the local lattice spacings from the mean lattice spacing, thus, resulting in peak broadening.

If the broadening is due to microstrains only, the mean lattice strain is given by

$$e = \frac{\beta}{4 \tan \theta} \quad [\text{Ref. 53}]. \quad (16)$$

Usually, however, both crystallite size and strain broadening effects are convoluted in the diffraction profile, and a means of deconvolution is required to determine the respective contributions to the integral breadth. Because of the difference in functionalities of D_v and e , with respect to θ , their contributions to β can be deconvoluted. From equation (14),

$$f(y) = \sum_n \left[F_r(n) \cos 2\pi n \left(\frac{y}{a} \right) + F_i(n) \sin 2\pi n \left(\frac{y}{a} \right) \right]. \quad (17)$$

Utilizing a Stokes deconvolution of the measured profile, the real and complex Fourier coefficients, of the diffraction profile $F_r(n)$ and $F_i(n)$, can be obtained using equation (13). Renaming $F_r(n)$ as A_n and $F_i(n)$ as B_n , Warren and Averbach were able to determine the complex coefficients as

$$A_n = \frac{N_n}{N_3} \langle \cos 2\pi l Z_n \rangle \quad (18)$$

and

$$B_n = -\frac{N_n}{N_3} \langle \sin 2\pi l Z_n \rangle \quad (19)$$

where:

$$N_n = \frac{N_n(\text{sample})}{N(\text{column})} = \frac{\text{no. of cells in the whole sample having an } n^{\text{th}} \text{ neighbor in the same column}}{\text{no. of columns in the sample}}$$

(which can be rewritten as N_n = the number of cells with an n^{th} neighbor in the same column), N_3 = the number of cells per column, n = the harmonic number, l = the order of reflection, a_3 = the unit lattice spacing perpendicular to the $00l$ reflections, $L = na_3$ = the

real space distance between a pair of n^{th} neighbors along a line perpendicular to the $00l$ planes, Z_n = the number (or fraction) of lattice spacings perpendicular to the $00l$ reflection by which the distance between a pair of n^{th} neighbors has changed due to distortion, $\Delta L = Z_n a_3$ = the change in distance between a pair of n^{th} neighbors due to distortion. With this result, the strain, ϵ_L , can be expressed as $\epsilon_L = \frac{\Delta L}{L} = \frac{Z_n}{n}$.¹

The parenthesis in equation (18) and equation (19) signify average values since no assumptions about the direction of relative displacements of the unit cells is made in the derivation. The cosine coefficient of equation (18) is the product of a size related term and a distortion related term as

$$A_n^{\text{size}} = \frac{N_n}{N_3} \quad (20.1)$$

and

$$A_n^{\text{distortion}} = \langle \cos 2\pi l Z_n \rangle \quad (20.2)$$

the former being dependent on the column length only (representing the size component), and the latter being dependent on the strain only (representing the distortion component). The cosine coefficient measured can now be represented by the product

$$A_n = A_n^{\text{size}} A_n^{\text{distortion}}. \quad (21)$$

¹The derivation of the Warren and Averbach analysis is begun from a general assumption that the sample is orthorhombic, with reflection from the $(00l)$ plane. It is assumed the sample is comprised of unit cells arranged in columns, with spacing $L = na_3$, between an arbitrary pair of unit cells located in a column whose axis is normal to the reflecting plane (see Figures 5 and 6). However, the analysis is completely general, and is applicable to all crystal systems and reflections from non- $(00l)$ type planes [Ref. 54].

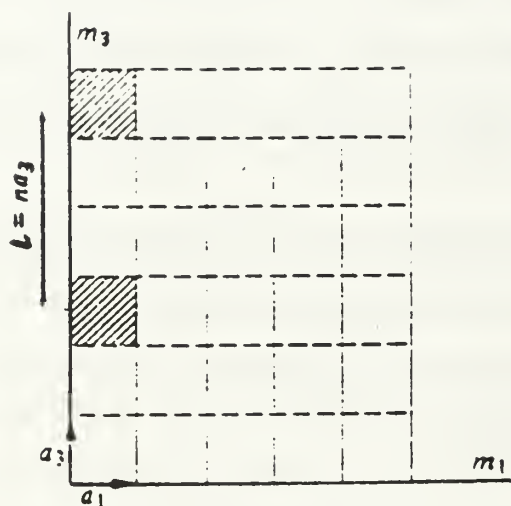


Figure 5. Real Space Representation of a Columnar Material used in the Warren Averbach Derivation [Ref. 55]

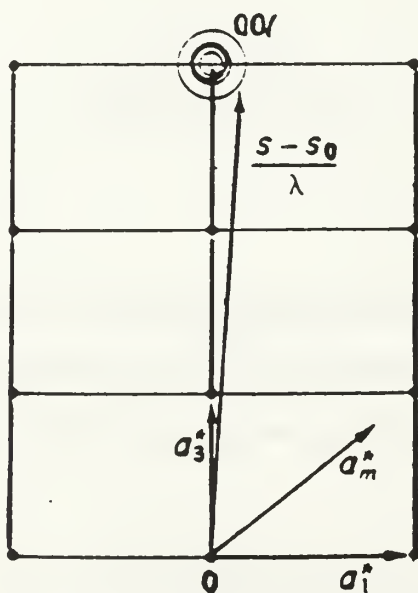


Figure 6. Reciprocal Space Representation of a $00l$ Reflecting Plane used in the Warren Averbach Derivation [Ref. 56]

Assuming multiple order reflections have been measured, (e.g. 001, 002, 003), and their respective Fourier coefficients have been determined, it is possible to separate the size coefficients, A_n^{size} , from the distortion coefficients, $A_n^{distortion}$, since the size coefficient is independent of l , whereas the distortion coefficients depends on l as well as the relative unit cell displacement Z_n . Assuming the product lZ_n is small, $\langle \cos 2\pi l Z_n \rangle \rightarrow 1 - 2\pi^2 l^2 \langle Z_n^2 \rangle$ which can be expressed in logarithmic form as

$$\ln \langle \cos 2\pi l Z_n \rangle = \ln(1 - 2\pi^2 l^2 \langle Z_n^2 \rangle) = -2\pi^2 l^2 \langle Z_n^2 \rangle. \quad (22)$$

Expressing equation (20) in its logarithmic form with substitution from equation (22), yields

$$\ln A_n(l) = \ln A_n^{size} - 2\pi^2 l^2 \langle Z_n^2 \rangle. \quad (23)$$

Plotting $\ln A_n(l)$ versus l^2 , gives a linear relation where the size coefficient, A_n^{size} is determined from the y-intercept, and the slope yields the value for $-2\pi^2 \langle Z_n^2 \rangle$. Figure 7 shows an example of such a plot. Since the change in displacement in the direction normal to the reflecting planes is given by $\Delta L = a_3 \langle Z_n \rangle$, and $L = na_3$ (refer to Figure 3), then

the strain can be expressed as $\langle \epsilon_L \rangle = \frac{\Delta L}{L} = \frac{\langle Z_n \rangle}{n}$, and $\langle Z_n \rangle^2 = \langle \epsilon_L^2 \rangle n^2$. Since n and l are known, the root mean squared (r.m.s.) strain $\langle \epsilon_L^2 \rangle_{meas}^{1/2}$ may be determined from the slope of the plots over several (at least two) orders of reflection and represents the r.m.s. strain in the direction normal to the reflecting plane. It must be remembered that the r.m.s. value so measured, actually represents the difference between the total residual strain at the microlevel and the long range residual strain. Thus, the calculated r.m.s. strain is a measure of the deviations of the local microstrain from the average long range residual strain in the sample. Mathematically this is given by

$$\langle \epsilon_L^2 \rangle_{\text{meas}} = \langle (\epsilon_{\text{tot}}^{\text{res}} - \epsilon_{\text{long range}}^{\text{res}})^2 \rangle = \langle (\epsilon_{\text{tot}}^{\text{res}})^2 \rangle - 2\langle \epsilon_{\text{tot}}^{\text{res}} \epsilon_{\text{long range}}^{\text{res}} \rangle + \langle (\epsilon_{\text{long range}}^{\text{res}})^2 \rangle. \quad (24)$$

Now,

$$\langle \epsilon_{\text{tot}}^{\text{res}} \rangle = \epsilon_{\text{long range}}^{\text{res}} + \langle \epsilon_L \rangle,$$

but, $\langle \epsilon_L \rangle = 0$, since if the positive and negative components of ϵ_L do not cancel one another, they will merely contribute to $\epsilon_{\text{long range}}^{\text{res}}$ and result in a peak shift, but no peak broadening. Therefore,

$$-2\epsilon_{\text{long range}}^{\text{res}} \langle \epsilon_{\text{tot}}^{\text{res}} \rangle = -2(\epsilon_{\text{long range}}^{\text{res}})^2$$

and

$$\langle \epsilon_L^2 \rangle_{\text{meas}} = \langle (\epsilon_{\text{tot}}^{\text{res}})^2 \rangle - (\epsilon_{\text{long range}}^{\text{res}})^2 \text{ [Ref. 58]}. \quad (25)$$

Thus, it is important to remember that the r.m.s. value of ϵ_L , which is obtained by the Warren-Averbach method, determines not the average strain, but rather, the deviation from the mean (long range) strain.

The method described achieves the desired separation using the real (cosine) Fourier coefficient, A_n , only, and is the traditional cosine method of arriving at the r.m.s. strain value. This method assumes that the origin of the Fourier series expansion is the centroid of the standard and measured profiles, and that each centroid location is known with high accuracy. If this is the case, the imaginary parts of the Fourier coefficients are small, resulting in reliable results. In practice, small deviations from the true centroid positions of the measured and standard profiles are likely to result (due to interference

between peaks or due to background errors) causing significant error to the calculated Fourier coefficients for the true (deconvoluted) profile [Ref. 59].

A second method, known as the modulus method, uses the modulus of the real and imaginary Fourier coefficients of the measured and structural profiles which make the location of the origin of the Fourier series expansion irrelevant. The discussion of the modulus method that follows is borrowed from [Ref. 60]. The modulus from equation (13) is defined as

$$|M(n)| = \left[(F_r(n))^2 + F_i(n)^2 \right]^{1/2}.$$

The derivation from this point is carried out in the same manner as the cosine method resulting in the relation

$$|M(n)| = A_n^{size} - A_n^{size} 2\pi^2 l^2 \left(\langle Z_n^2 \rangle - \langle Z_n \rangle^2 \right).$$

A plot of $|M(n)|$ versus l^2 yields A_n^{size} as in the cosine method, and the value $\{\langle Z_n^2 \rangle - \langle Z_n \rangle^2\}^{1/2}$ which can be expressed, as in the case of the cosine method, as $n\{\langle \epsilon_L^2 \rangle - \langle \epsilon \rangle_L^2\}^{1/2}$. Since $\langle \epsilon_L \rangle = 0$ as before,

$$\left\{ \left\langle (\epsilon_{\text{tot}}^{\text{res}})^2 \right\rangle - (\epsilon_{\text{long range}}^{\text{res}})^2 \right\}^{1/2} = \langle \epsilon_L^2 \rangle_{\text{meas}}^{1/2}$$

which represents the r.m.s. strain. The particle size is determined in the same manner as the cosine method discussed below.

For the determination of crystallite size, the values of A_n^{size} as a function of harmonic number, n , are read off from the plot of $\ln A_n$ versus l^2 (Figure 7). Then A_n^{size} is plotted against n , as shown in Figure 8. It can be shown that when $n \rightarrow 0$,

$$\left(\frac{dA_n^{size}}{dn} \right)_{n \rightarrow 0} = -\frac{1}{N_3}. \quad (26)$$

Therefore, the slope of the A_n^{size} versus n plot at $n=0$ equals $-\frac{1}{N_3}$, N_3 being the n axis intercept of the slope of the A_n^{size} versus n curve at $n \rightarrow 0$. The average column length perpendicular to the $00l$ planes (i.e., the crystallite size) is then given by $N_3 a_3$, where a_3 is the unit displacement along the column length.

The Warren-Averbach approach can be generalized to any order of reflection by powder diffraction. For cubic systems equation (23) can be expressed as

$$\ln A_L(h_o) = \ln A_L^{size} - \frac{2\pi^2 \langle \epsilon^2 \rangle L^2 (h^2 + k^2 + l^2)}{a^2} \quad (27)$$

where: d is the interplanar spacing, L is a real space distance along the columns of cells perpendicular to the reflecting planes, and a is the lattice constant. A graph of this relation is shown in Figure 9, where the abscissa intercept of the initial slope represents the average column length, $\langle D \rangle$, perpendicular to the reflecting planes.

Observation of actual A_n^s versus n plots sometimes show a concave downward line near $n = 0$, which has come to be known as the "hook effect" [Ref. 63]. Since the second derivative of A_n^s with respect to n (i.e., $\frac{d^2 A_n^s}{dn^2}$) can only be positive, the plot of A_n^s versus n can be concave upward but never concave downward. This situation is graphically represented in Figure 9 by the dashed line. The source of this problem can be traced to using line profile backgrounds in the Fourier analysis that are too high, leading to

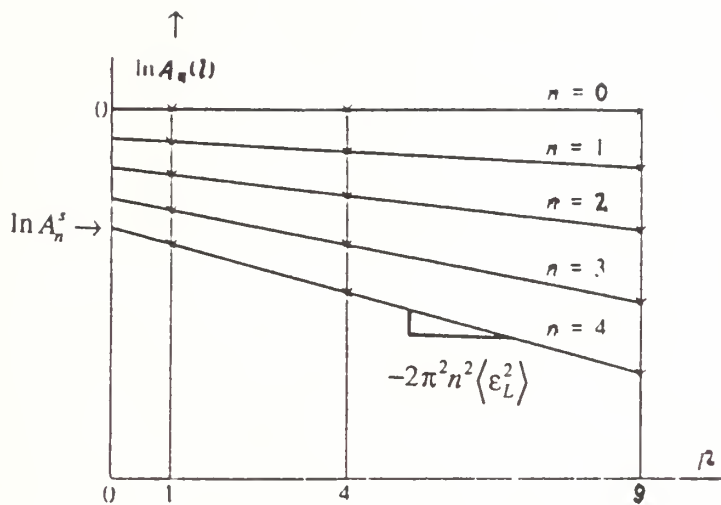


Figure 7. Plot of $\ln A_n^s(l)$ vs. l^2 [Ref. 57]

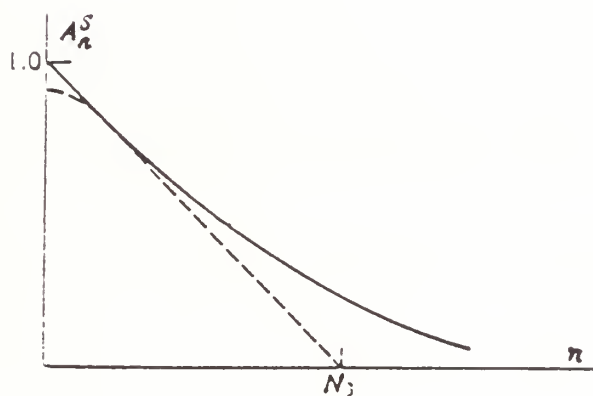


Figure 8. Plot of A_n^s vs. n [Ref. 61]

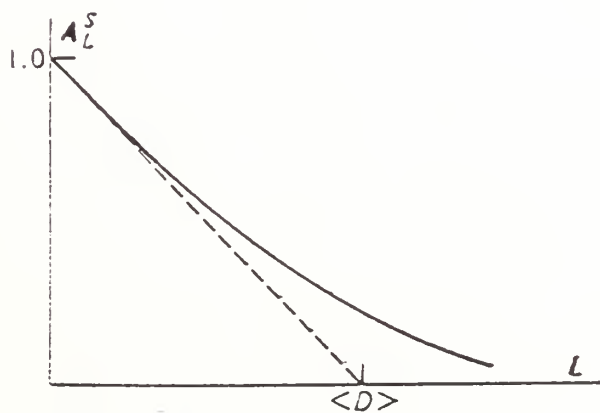


Figure 9. Plot of A_L^s vs. L [Ref. 62]

unintended peak interference. There are many graphical schemes to work around this problem, but so far, no formal way has been developed. The easiest way, is to merely extrapolate the near linear portion of the curve back to the ordinate and base calculations on this value. If a graphical option is not used, then background adjustment is the only other way to avoid this effect.

The Warren-Averbach method, therefore, allows the determination of particle size and strain contribution to line broadening independently and simultaneously. Though the manual calculations are laborious, with the use of computer driven software currently available on most diffractometer systems, these calculations can be done in a matter of minutes requiring only the input of the standard diffraction profile and the measured diffraction profile.

In the above analysis, it was assumed that peak broadening occurs due to particle size and strain effects only, ignoring any contributions from deformation or twin faults.

C. PHYSICAL SIGNIFICANCE OF THE RESULTS OBTAINED FROM THE WARREN-AVERBACH ANALYSIS

As discussed previously, small particle size can contribute to line broadening. If the sample was completely free from dislocations and stacking faults, the true particle size could be determined directly from a broadened profile. In reality, dislocations can be present, to a high degree, in random or non random configurations. If the dislocations are known to be dispersed randomly throughout the material, a measure of the particle size would be an indication of the dislocation density of the material. However, dislocations that are not randomly dispersed in grains and form low angle grain boundaries further subdivide the grain into smaller subgrain regions leading to a lower realized particle size and further line broadening. Additionally, dislocation lines break up the ordered planar

structure causing slight disorientation between planes resulting in a range of angles satisfying the Bragg condition which causes line broadening. If dislocations are known to be distributed in non random fashion so described, the particle size obtained would be representative of the subgrain size. The particle size determined from the Warren-Averbach method must therefore be corroborated with transmission electron microscopy (TEM) studies of the actual film microstructure. TEM corroboration of the density of stacking faults and twins should likewise be conducted.

Assuming that a film is free of dislocations, an applied stress would cause a uniform change in planar spacing, resulting in a peak shift. The total strain in the sample would then be the long range strain, from which the residual stress in the film could be calculated. In the presence of dislocations dispersed in the material, however, local strain fields may deviate from the long range value. Usually, both positive and negative stress states will be found locally due to the presence of dislocations. Even if the average of these stresses equals zero, and no peak shift is noted, the r.m.s. value of strain as measured by the Warren-Averbach method may be non-zero. The Warren Averbach analysis yields a value of strain which represents the difference between the sum of the positive and negative microstrains squared minus the long range (or average) strain squared. This result then shows the possible microstrain deviation from the average strain, not the average strain itself. The stress calculated from this result, therefore represents the possible stress deviation from the residual stress present in the film. Although it is not a measure of the true residual stress, it is none the less useful as a measure of the degree of plastic deformation of the film, which may, under certain circumstances, yield a measure of interfacial adhesion.

Consider two film-substrate pairs, both Au-AlN, the first with better interfacial adhesion than the second due to differences in substrate surface treatment prior to

metallization. Although the product $(\Delta\text{CTE})(\Delta T)$ for the given materials system is the same for both pairs, differences in the strains induced in the films are expected because of different degrees of strain accommodation at the interfaces. If plastic deformation occurs in the films during cooling, the stresses induced can be relaxed to a level below the yield strength by dislocation generation. The residual strain/stress measured via peak shift based techniques represents the relaxed value. If both samples underwent the same extent of plastic deformation, then the stress measured by peak shifts would be indicative of the interfacial adhesion. However, in general, the extent of plastic deformation can be substantially different between the two samples, and no direct correlation between the interfacial adhesion and the long range residual stress/strain measured by peak shift is obtainable.

The r.m.s. strain measured based on peak breadth, on the other hand, represents the deviation of the local microstrains from the long range value, and thus, is indicative of the extent of plastic deformation of the film. For a constant $(\Delta\text{CTE})(\Delta T)$, the extent of plastic deformation is a function only of the interfacial adhesion between the film-substrate pair. Therefore, the r.m.s. strain is likely to provide an indirect measure of the quality of interfacial adhesion. The condition for development of a thin film metallization procedure would be to produce a film with good adhesion and a low value of the mean long range strain. Having a low strain would prevent cracking of the film during use, whereas, good interfacial adhesion would prevent peeling of the film at its interface. The existence of a low strain condition, however, does not necessarily go hand-in-hand with good adhesion, requiring both the long range strain and adhesion to be evaluated independently. The long range stress/strain can be evaluated non-destructively using techniques such as "the $\sin^2 \psi$ " measurement method [Ref. 64]. However, nondestructive evaluation of interfacial adhesion is not feasible at present. It is proposed that while adhesive properties cannot be

measured directly with any presently available x-ray based technique, the Warren-Averbach method may provide an indirect evaluation of the extent of interfacial adhesion, and therefore is a useful tool in studying the quality of metallizations.

III. EXPERIMENTAL

A. MATERIALS

The AlN substrates were produced and provided by W.R. Grace and Company at a purity level of 99.9%. The AlN was sintered using CaO as a sintering aid. An XRD scan of the substrates revealed no Ca-aluminate peaks that would otherwise interfere with the Au (111) diffraction line after metallization, suggesting that the CaO resulting from the sintering aid additions, was lost during processing.

The Au used for metallization was obtained from The Aldrich Chemical Company and was used in the powder form for metallizations. The Au powder had a purity level of 99.99% and an average particle size of <44 microns (-325 mesh). This powder was also used to prepare the Au standard, since the powder size was sufficiently large (greater than 1 micron) so as to prevent particle size broadening of the standard peaks [Ref. 65].

B. EQUIPMENT

1. Evaporator Chamber and Sub Components

A schematic of the thin film evaporation system is shown in Figure 10. The chamber was made for metallizations under HV conditions. Six vacuum service ports with o-ring seals allow for a variety of peripheral equipment and monitoring devices to be used during metallization. Of the three bottom ports, one was used merely as a viewing window and the two remaining ports were used for power feed-throughs. An external power supply was used to supply up to 40 AC amps, single phase, current to the power feed-throughs. The power supply was equipped with an output amp meter and rheostat that allowed for the precise control of current. This allowed the operator to control the

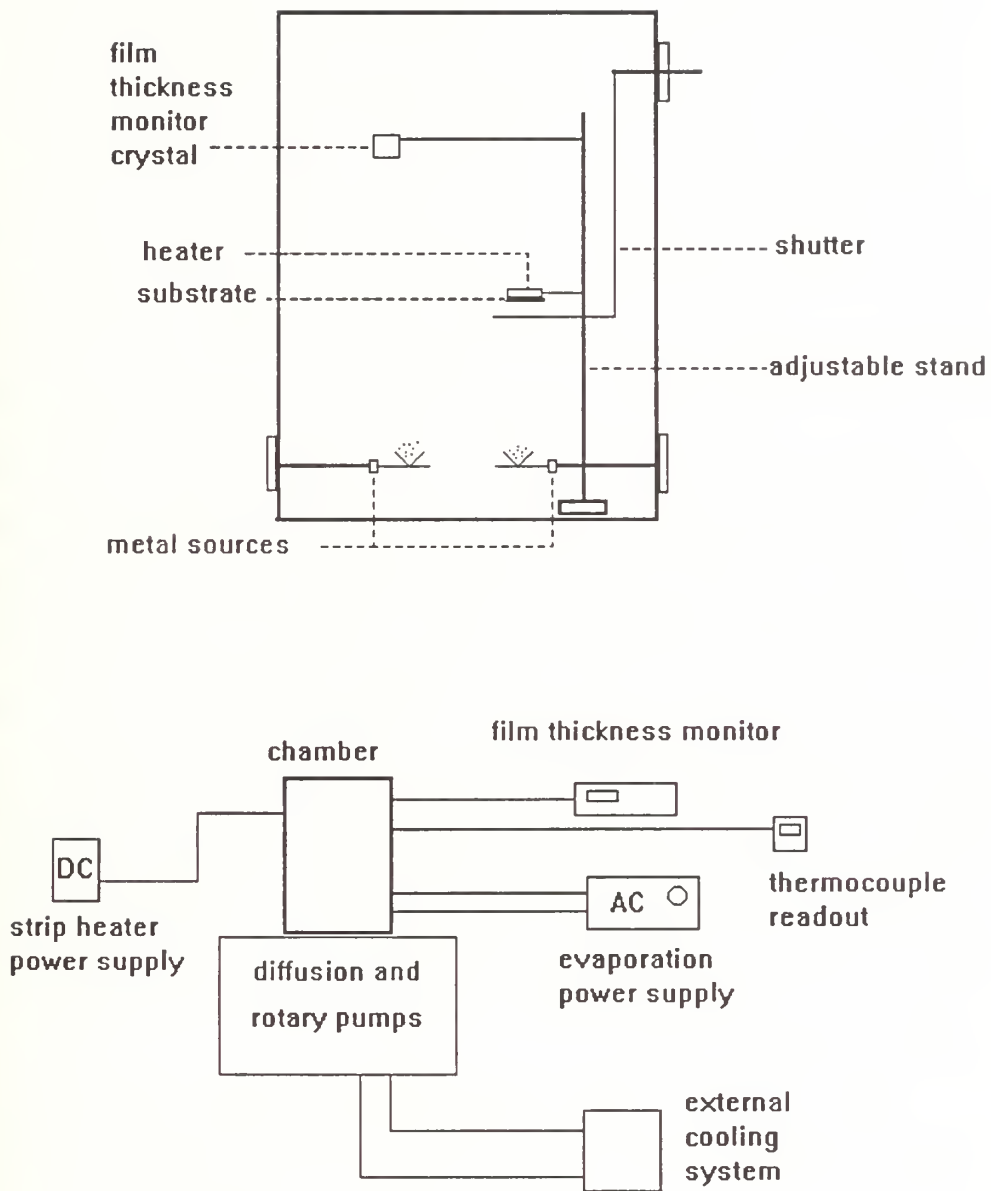


Figure 10. Chamber Layout and Equipment Block Diagram

metal deposition rate. Heavy gage leads with friction type disconnects permitted the power supply leads to be quickly changed to either feed-through. Resistive heating, provided the necessary heat to cause evaporation (sublimation) of the coating metal. The coating metal was held in tungsten foil boats which were clamped to the power feed-throughs. The upper ring of three service ports housed a rotary shutter shield to cover the substrate when applying power to the feed-throughs. This enabled any oxides or hydrocarbons to be burned off the coating metal prior to actually depositing the metal on the substrate surface. Once the burnoff was completed, the shutter could be rotated out of the way to expose the substrate surface. The second upper service port housed the film thickness monitor coaxial cable feed-through. The remaining upper service port housed a combination electrical feed-through which passed a K type thermocouple lead for monitoring the substrate surface temperature during metallization, and two DC power leads used to supply power to a small mica heater unit. The mica heater unit capable of heating the substrate up to 500°C during metallizations. The substrate itself was physically clamped to the heater backing plate and held at the desired position by a small, adjustable stand located inside the chamber. All seals were made with rubber o-rings coated with high vacuum grease.

The high vacuum needed to perform metallizations was achieved by use of a diffusion pump which was capable of reaching vacuum levels as low as 5×10^{-7} torr under ideal conditions. Continuous pressure readings of the vacuum during metallizations was provided by use of a Penning gage with a digital readout.

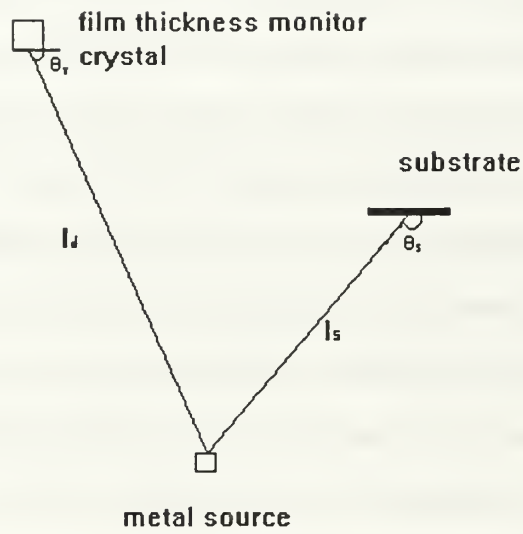
2. Film Thickness Monitor

The film thickness monitor provided instantaneous readings of the film thickness during metallizations. The film thickness monitor, supplied by Cressington Inc., used a pizo-electric quartz crystal located inside the chamber. The signal developed was sent

through the coaxial cable to a processing unit with a digital readout. Since the oscillating characteristics of the crystal is a function of the coating metal density, the density of the coating metal was required as an input to the film thickness monitor processor prior to deposition. Additionally, the location of the crystal (distance and angular separation) with respect to the substrate and the coating source, greatly affected the thickness readings obtained. This geometry effect was accounted for by use of a scaling factor, called a tooling factor, which was also a required input to the thickness monitor processor. Figure 11 shows the key dimensions and angles which required accurate measurement in order to calculate the correct tooling factor. The film thickness monitor processor used was a two channel device that allowed two different coating metals to be monitored during deposition. The two channel feature was necessary in order to monitor the inter-layer thickness as well as the Au film thickness.

As shown in Figure 11, the distances, l_s and l_d , greatly influenced the magnitude of the tooling factor. Selection of the correct sample-to-source distance, l_s , and the crystal-to-source distance, l_d , was critically important in other regards as well:

- (1) Too small a value of l_s resulted in splattering of the coating metal on the substrate surface,
- (2) Too small a value of l_d resulted in the rapid coating of the crystal face to the point that the crystal was rendered useless before achieving the desired film thickness,
- (3) Too large a value of l_s resulted in expenditure of a large amount of coating metal, greatly lengthening the time required to coat the substrate which resulted in excessive heating of the chamber and erroneous thickness readings. Unfortunately, the optimum values of l_s and l_d had to be obtained through trial and error. In addition, the optimum distances differed significantly depending on the coating metal used. For the



The tooling factor is calculated by:

$$T.F. = \left(\frac{l_d}{l_s} \right)^2 \left(\frac{\sin \theta_s}{\sin \theta_d} \right)$$

Figure 11. Calculation of the Tooling Factor From Metallization Geometry [Ref. 66]

metals used in this study, an l_s of 10.7 cm and an l_d of 28.0 cm were found to be satisfactory for metallization.

C. PROCEDURE

1. Gold Standard Preparation

Preparation of an Au standard was necessary to obtain the instrumental profile used in the Warren-Averbach analysis as discussed previously. The Au standard was prepared by annealing a sufficient amount of the Au powder in flowing Argon at 300°C for three hours in an alumina crucible. After air cooling, it was found that the Au particles had sintered together. To break up the particles, the Au powder was shaken in an ultrasonic vibrator and then sieved using a 325 mesh sieve onto a low noise, quartz XRD sample holder. Adhesion of the powder to the sample holder was achieved by using a thin film of high vacuum grease. A glass slide was then lightly pressed over the powder to assure that the powder was as flat as possible.

2. Substrate Surface Preparation

Table 2 identifies the samples by number and provides a metallization summary.

TABLE 2. SUMMARY OF SURFACE TREATMENTS

SAMPLE NAME	BASE PRESS. torr	SURF. ROUGH. microns	INTER-LAYER metal/nm	OXIDE LAYER microns	TEMP. DURING DEP. deg C	BAKED (Prior to Coating)	FINAL THICK. nm
AUALN1	5×10^{-6}	20-25	NONE	NONE	25-60	NO	327
AUALN2	5×10^{-6}	15	NONE	NONE	25-60	NO	328
AUALN3	5×10^{-6}	1	NONE	NONE	25-60	NO	328
AUALN4	4×10^{-6}	1	Cr/6.4	NONE	25-60	YES	310
AUALN5	6×10^{-6}	1	Ti/7.7	NONE	25-60	YES	320
AUALN6	4.5×10^{-6}	1	NONE	NONE	25-60	YES	327
AUALN7	4.5×10^{-6}	1	NONE	3.0	25-60	YES	327
AUALN8	6×10^{-6}	1	Cr/6.3	NONE	95-140	YES	329
AAU1	5×10^{-9}	20-25	NONE	NONE	25-60	NO	450

Prior to preparing the substrate surfaces, the AlN substrates were cut to a dimension that would fit directly in the XRD sample holder using a diamond saw. The surface roughness condition of the AUALN1 and AAU1 samples were used "as received" and estimated to be between 20 and 25 microns. No other treatments were applied to these two samples. The AUALN2 sample was prepared using first 400 then 600 grit abrasive paper with de ionized water. The remaining samples, having a surface roughness of 1 micron, were prepared by using 400 and 600 grit abrasive paper, followed by polishing with 6 micron, then 1 micron diamond paste. Prior to metallization, all samples were thoroughly washed with acetone followed by ultrasonic sink cleaning in ethanol.

The AUALN7 sample was oxidized using the procedure of [Ref. 67]. The AlN substrate was placed in a fused silica holder and heated to 1000°C using a dilatometer oven. Clean, dry oxygen was supplied at a flowrate of 20 ml/hr (resulting in a linear flowrate of about 40 mm/min) for a period of 15 hours. A thermocouple was used to monitor the substrate temperature during oxidation. Based on these conditions, an oxide layer of about 3 microns was produced on the substrate surface.

3. Metallization Procedure

After preparing and cleaning the substrate surfaces, the substrates were clamped to a combination sample holder/heater assembly in the vacuum chamber. Vacuum was then drawn in the chamber with the diffusion pump. An average vacuum of 5×10^{-6} torr was achieved during all metallizations with the exception of the AAU1 sample which was prepared at 5×10^{-9} torr in a separate UHV chamber. A thermocouple attached to the sample holder was placed in contact with the edge of the substrate which allowed for the continuous monitoring of the substrate temperature during metallization. The rotary shutter was then inserted, isolating the substrate from the metal source. Power was supplied to each power feed-through to burn off any oxides or hydrocarbons from the

coating metal. The strip heater was energized, using a variable DC power supply, until the substrate was heated to 300°C for a period of 30 minutes. This baking procedure was used on all samples except samples AUALN1 through AUALN3, since the heater unit was not available when these samples were prepared. The baking was performed as a precaution to remove any trace amounts of hydrocarbons on the substrate surface prior to coating. With the exception of the AUALN8 sample, the substrate was allowed to return to a temperature of 25°C. The AUALN8 sample was allowed to cool to 95°C to investigate the substrate surface temperature effect on film quality. The rotary shutter was then removed and the metallization of the substrate was performed.

Inter-layers of Cr and Ti (samples AUALN4, AUALN5 and AUALN8) were made during the metallization process by using one of the two power feed-throughs to deposit the inter-layer metal. The remaining power feed-through was then used to deposit the Au film. Since two power feed-throughs were available, chamber vacuum did not have to be broken between the deposition of the inter-layer metal and the Au film. This prevented the oxidation of the inter-layer surface prior to applying the Au film.

During the inter-layer and Au metallizations, an average deposition rate was 280 angstroms per minute was used. A deposition temperature for samples AAU1 and AUALN1 through AUALN7 was maintained between 25 – 60°C. Deposition temperature for the AUALN8 sample was maintained between 95 – 140°C.

Once metallization was complete, the rotary shutter was inserted prior to breaking chamber vacuum, to prevent blowing debris onto the freshly coated substrate surface.

D. XRD PROCEDURES

1. Parameters For XRD Scanning

Following metallization, the samples were loaded directly into the diffractometer. A Philips XRG 3100 X-ray generator with a copper target, a bent graphite monochromator and a Digital Systems data control and processor were used to perform the scans. Goniometer scans were performed using a step size of 0.01 degrees (2-theta) for 4 seconds. Tube voltage was maintained at 30 kv with a tube current of 35 milliamps. The same settings were used to scan the Au standard and all samples.

2. Post XRD Scan Processing

Following the XRD scans, the raw data scan files generated were analyzed using a APD 1700 software package developed by Philips. The capabilities of this software enabled the raw data to be processed in a way suitable for a Warren-Averbach analysis described earlier. Specific software capabilities discussed below, were taken from [Ref. 68].

The first step of the analysis, called the Pattern Treatment module, was used to separate crystalline peaks from amorphous peaks. Next, K-alpha 2 lines and background were removed and a new file was generated. At this point, the operator had the option to modify the new file, by selecting an intensity level below which the system ignored any intensity information. This feature enabled the operator to filter out any background noise spikes. It was found that this parameter played a major role in obtaining good profile fits of the raw data.

Following the Pattern Treatment phase of the analysis, the raw data files developed were used to generate a mathematical profiles of the (111) and (222) Au peaks occurring in the coated AlN samples. This part of the analysis, called Profile Fitting module, employed a Marquardt non-linear least squares algorithm to fit the profiles.

Profile fitting was necessary to separate the peak overlap between AlN and Au peaks. Figures 12 and 13 show diffraction scans of the Au standard and AlN prior to metallization. Note that both the (111) and (222) peak positions for Au had interfering AlN peaks that required separation before the Warren-Averbach analysis could be performed. The Profile Fit module generated profiles for both the AlN and the Au peaks present. After the profiles were generated, the operator could super impose the Au and AlN profiles onto the raw data scan as well as any residual peaks that were "mathematically" left over from the profile fitting process. The goodness of fit was checked by observing the intensity of the residual peaks in the 2-theta range of interest. If the residuals showed low intensities over the 2-theta range of interest, (i.e., if no peaks other than the expected AlN peak and the expected Au peak were apparent), the fit was considered good. Figures 14 and 15 show the result of this procedure for an Au (111) peak and a (222) peak respectively. It can be seen from Figures 14 and 15 that only a AlN peak and a Au peak are present and no others. The profile fitting method was largely trial and error, using the desired 2-theta range, peak intensity, peak position and background as input parameters. Once satisfactory profiles were developed for both the Au (111) and (222) peaks, they were stored in separate files to be used in the Warren-Averbach phase of the analysis.

The Warren-Averbach module used the Au (111) and (222) profiles of a sample as well as the (111) and (222) peaks of the Au standard and performed the Warren-Averbach deconvolution using either the cosine method or the modulus method. Both methods were used in this study and compared. Particle size and r.m.s. strain are the output values. In this module, corrections for instrumental errors, the Lorentz-Polarisation factor, the K alpha-2 component and background corrections were applied. Once the corrections were applied, the deconvolution process for the low order ((111)

peaks) was executed. The program performed a Fast Fourier Transform (FFT) on both peaks followed by a Stokes deconvolution algorithm. The Fourier coefficients for the true profile were then computed and stored. The entire process was repeated for the high order (222) peaks. Once the Fourier coefficients for both order reflections were obtained, the module performed the necessary calculations and determined the particle size and r.m.s. strain values for the sample. A hook correction, if needed, was performed using an automatic method or a manual method.

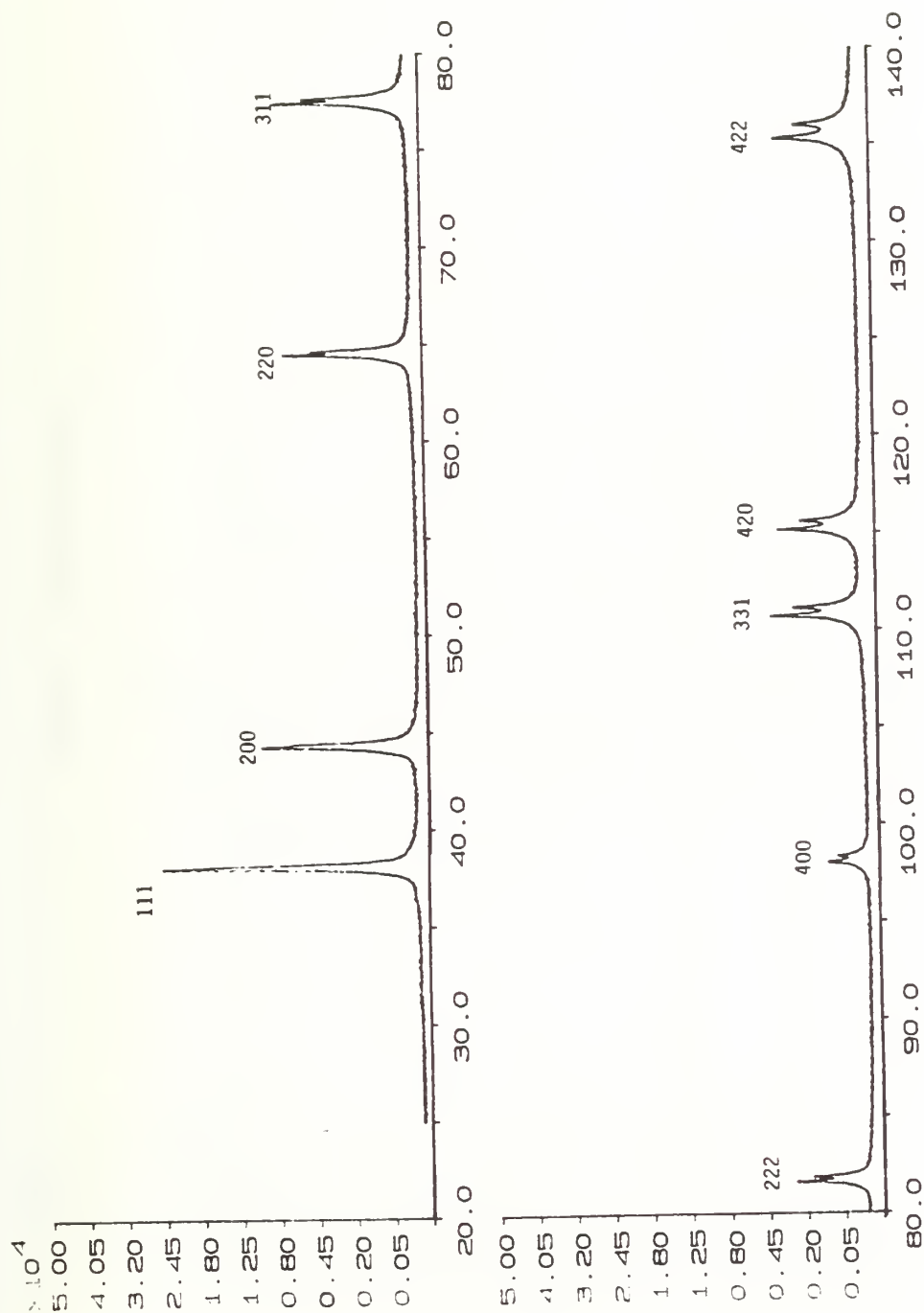


Figure 12. XRD Scan of Gold

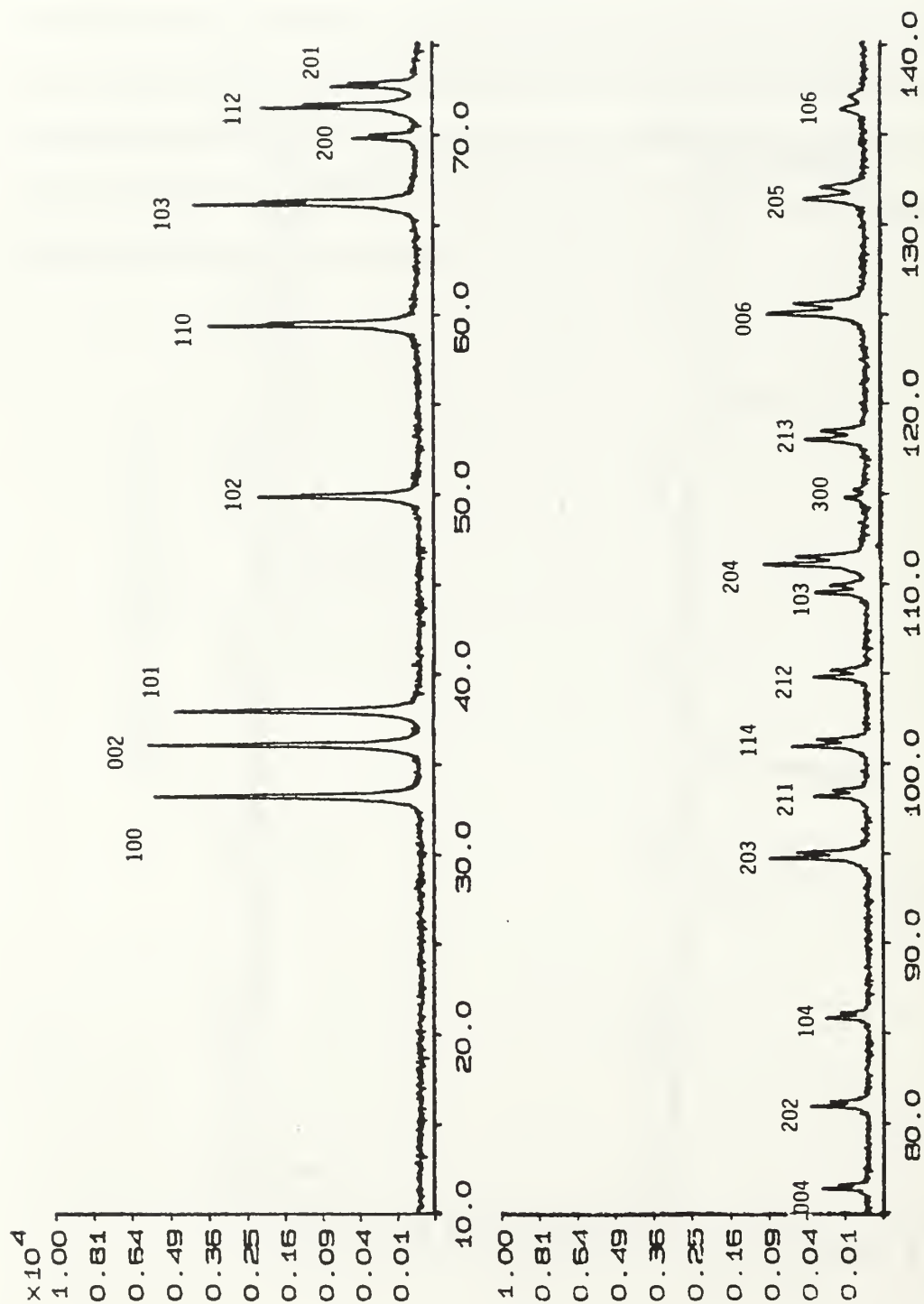


Figure 13. XRD Scan of AlN

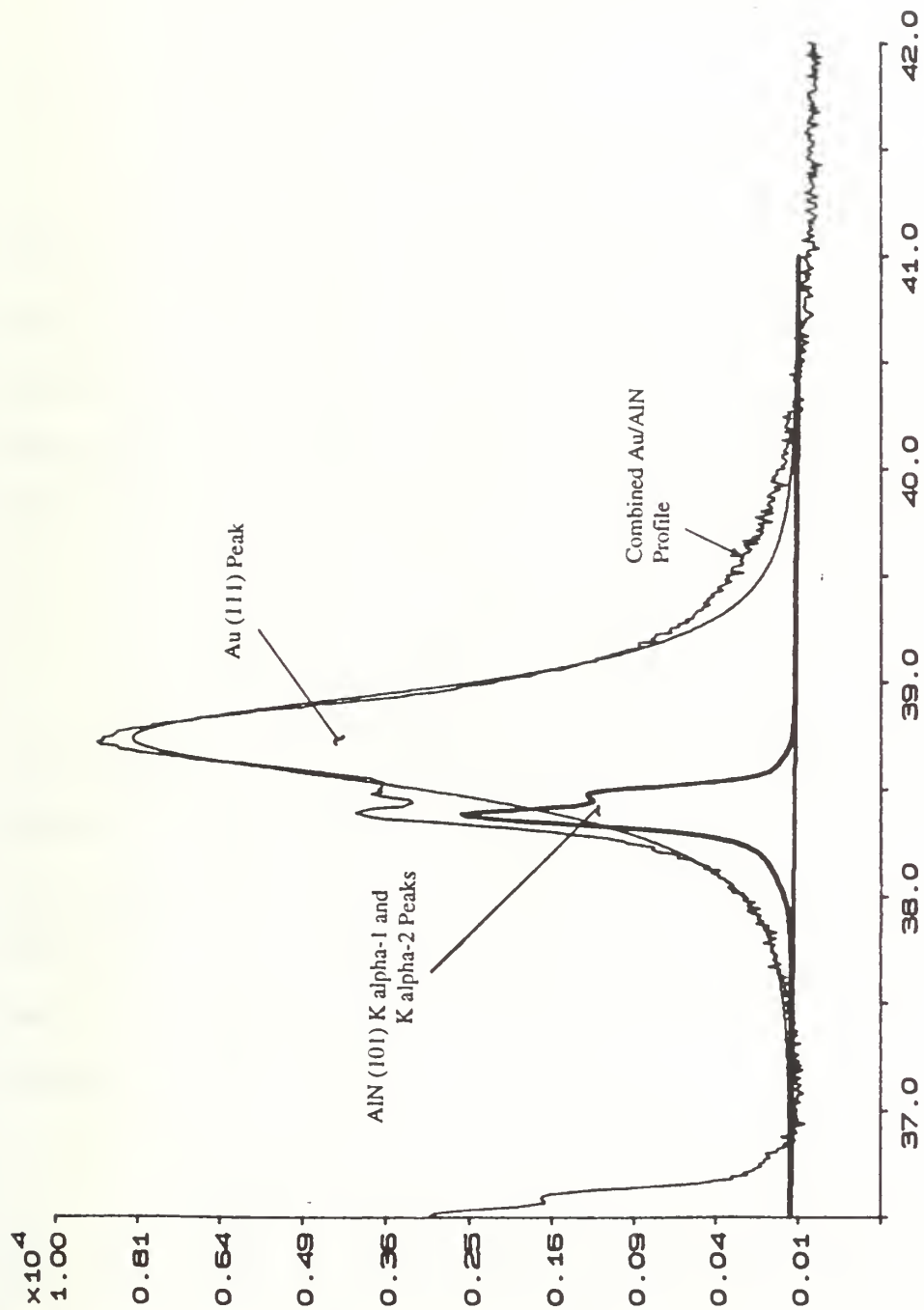


Figure 14. Separation of the Au (111) Peaks

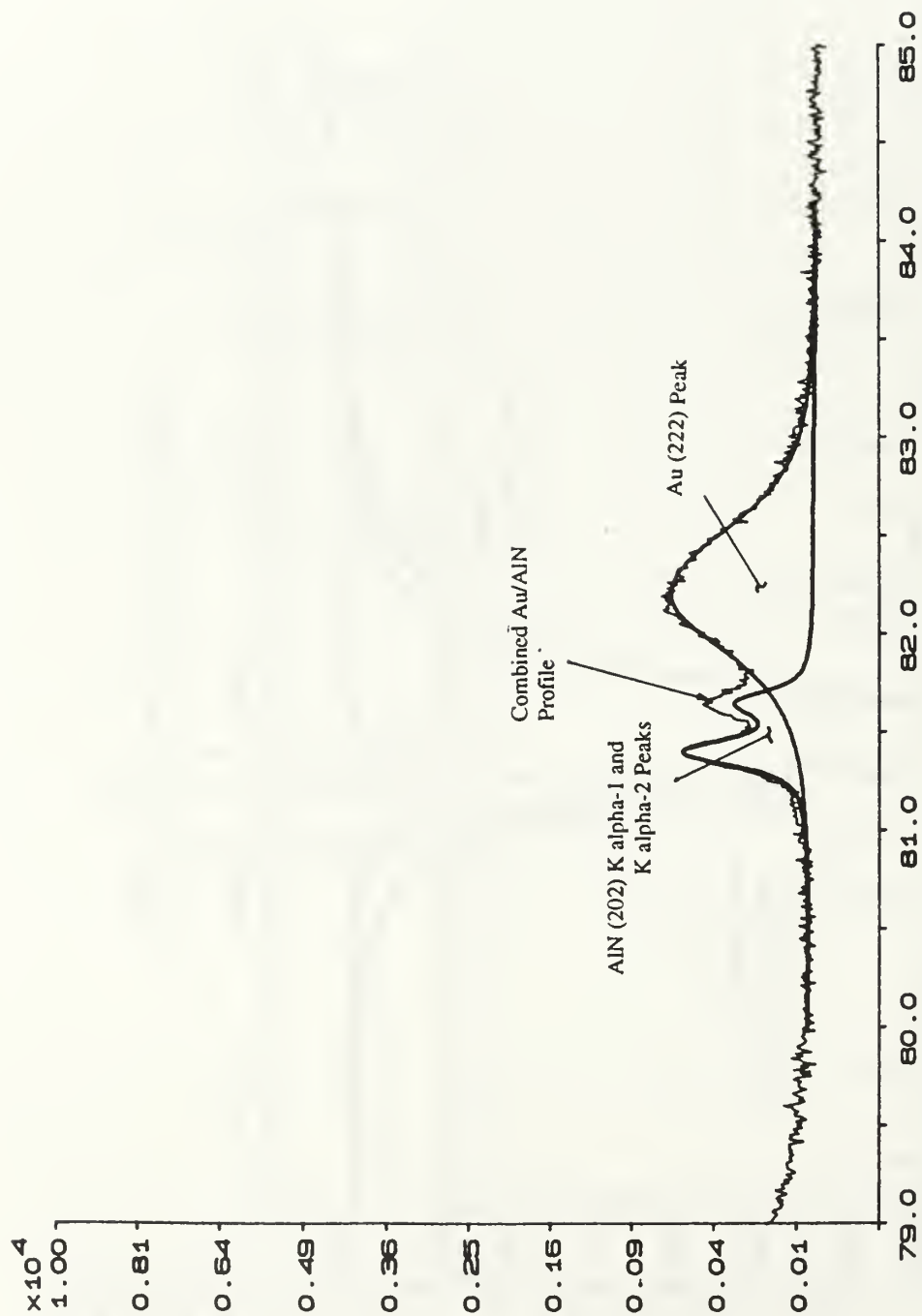


Figure 15. Separation of the Au (222) Peaks

IV. RESULTS AND DISCUSSION

A. RESULTS SUMMARY

1. R.M.S. Strain, Particle Size and Stress Deviation

Table 3 lists the results of the particle size and r.m.s. strain obtained by the Warren-Averbach analysis. Results are shown for both the cosine method and the modulus method and show fairly good agreement for all samples. Table 3 also lists the stress deviation which was calculated based on [Ref. 69]. This method assumes that the stress state of the film is simply biaxial, since the film thickness is very small with respect to film length and width. The biaxial stress equation used for this calculation is

$$\langle \sigma_{dev} \rangle = \frac{E}{2\nu} \langle \epsilon_L \rangle_{meas}$$

where: $\langle \sigma_{dev} \rangle$ represents the possible stress deviation from the mean stress, E is Young's Modulus, ν is Poisson's ratio and $\langle \epsilon_L \rangle_{meas}$ is the r.m.s. strain. Values for Young's Modulus and Poisson's Ratio were taken from [Ref. 70] and represent thin film values vice bulk values. The values of r.m.s. strain found in this study are of the same order of magnitude as r.m.s. strains reported in other studies [Ref. 71] for Au films of roughly the same thickness.

2. Discussion

Considering the surface roughness results (AUALN1, AUALN2 and AUALN3), it was observed that as the surface roughness of the substrate was increased, the r.m.s. strain increased. Since this series of films were made under the same metallization conditions and involve the same materials, the $(\Delta CTE)(\Delta T)$ for each sample was the same.

TABLE 3. SUMMARY OF RESULTS

Sample Name	Surface Treatment	By		Cosine		Method		By	Moduli		Method	Δ Ther.		Ex. Coef.
		R.M.S. Strain %	R.M.S. Stress MPa	R.M.S. Stress MPa	Particle Size \AA	Particle Size \AA	Particle Size \AA		R.M.S. Strain %	R.M.S. Stress MPa		$\Delta\text{CTE}_1 \times 10^{-6} \text{ K}^{-1}$	$\Delta\text{CTE}_2 \times 10^{-6} \text{ K}^{-1}$	
AUALN1	20-25 μ , unox., RT	0.171	46.6	46.6	160.3	160.7	160.7	0.164	44.7	44.7	160.7	9.9	~	~
AUALN2	15 μ , unox., RT	0.140	38.2	38.2	239.5	265.7	265.7	0.135	36.8	36.8	265.7	9.9	~	~
AUALN3	1 μ , unox., RT	0.117	31.9	31.9	224.6	235.9	235.9	0.117	31.9	31.9	235.9	9.9	~	~
AUALN4	1 μ , unox., Cr, RT	0.163	44.4	44.4	205.4	222.4	222.4	0.155	42.2	42.2	222.4	1.7	8.2	8.2
AUALN5	1 μ , unox., Ti, RT	0.100	27.3	27.3	198.6	203.6	203.6	0.091	24.8	24.8	203.6	4.2	5.7	5.7
AUALN6	1 μ , unox., RT	0.167	45.5	45.5	253.1	263.1	263.1	0.162	44.2	44.2	263.1	9.9	~	~
AUALN7	1 μ , oxidized, RT	0.129	35.2	35.2	172.9	177.6	177.6	0.125	34.1	34.1	177.6	2.8	6.9	6.9
AUALN8	1 μ , unox., Cr, 95°C	0.115	31.3	31.3	262.1	268.1	268.1	0.116	31.6	31.6	268.1	1.7	8.2	8.2
AAU1	20-25 μ , unox., RT, UHV	0.195	53.1	53.1	183.9	190.3	190.3	0.193	52.6	52.6	190.3	9.9	~	~

Notes: (1) ΔCTE_1 values indicate the difference in the thermal expansion coefficients between the substrate and the metal adjacent to the substrate. ΔCTE_2 , where applicable, represents the difference in the thermal expansion coefficients between the interlayer metal and the Au film.

(2) RT indicates the substrate was metallized starting from room temperature.

This indicates a greater extent of plastic deformation occurs on rougher substrates and may indicate that adhesion improves as the substrate surface roughness is increased. A likely explanation for this behavior is that better mechanical interlocking is possible between the film and the substrate as surface roughness increases. This interlocking reduces the degree of strain relaxation possible by interfacial sliding, thereby, enhancing the extent of plastic strain.

The two samples metallized under different vacuum conditions (AUALN1 and AAU1) are considered next. Both samples had the same surface roughness and were metallized under the same conditions with the exception of the metallization pressure. The AAU1 sample (metallized under UHV conditions) had an r.m.s. strain significantly higher than the AUALN1 sample (metallized under HV conditions), indicating that more plastic deformation occurred in the film deposited at a lower base pressure. Since the same materials were used, it is suspected that the adhesion improves as metallization pressure is reduced. A possible explanation for this behavior is that less contamination of the substrate surface occurs at lower metallization pressures, resulting in better interfacial bonding. Other studies of copper films have borne this out [Ref. 72]. Additionally, lower metallization pressures are known to promote better epitaxial film growth, which may be related to the degree of interfacial bonding.

Analysis of the interlayer results is a bit more complex since two interfaces need to be considered. If the interlayer is assumed to act as a compliant layer (i.e., provides no resistance to the shrinkage of the applied film during cooling), then no stress could be transferred from the interlayer to the film. If the interlayer acts as a separate entity, then the differences in the CTE's between the interlayer and the film should account for the degree of plastic deformation, hence, the degree of r.m.s. strain observed. Finally, the interlayers may be considered to be merely surface modifiers, since the thickness of the

interlayer is very small compared to the film thickness. If interlayers do act as surface modifiers, then the $(\Delta\text{CTE})(\Delta T)$ effect between the interlayer and the film is not considered, and the presence of the interlayer either improves or degrades interfacial bonding between the film and the substrate in some fashion.

Analysis of the samples with inter-layers (AUALN4, AUALN5 and AUALN8) show significant, measurable r.m.s. strain values, indicating that the inter-layers probably do not act as compliant layers. The Au/AlN sample with a Cr inter-layer (AUALN4) displays a higher r.m.s. strain than the Au/AlN sample of the same surface roughness without any inter-layer (AUALN6), although the CTE mismatch between Au and Cr is less than that between Au and AlN. Therefore, it is unlikely that the inter-layers act as separate entities. This is reasonable since the inter-layers used were very thin, $\sim 60 - 70 \text{ \AA}$, and would not be expected to act as substrates. It is believed that the inter-layers act as surface modifiers, either by altering the nature of chemical bonding between Au and AlN at the interface, or by forming good chemical bonds with both the film and the substrate materials. The results show that the r.m.s. strain in the Au film is significantly larger for the sample with the Cr inter-layer than for the sample without any inter-layer, indicating that Cr promotes interfacial adhesion. The exact reasons for this is not known and would require further study. It is suspected that Cr has a high affinity toward oxygen, and any oxygen which may have been absorbed on the surface of the AlN could result in good bonding between Cr and AlN whereupon strong metallic bonds could be formed between Cr and the Au film. Likewise, it has been reported that Ti forms nitrides at the interface with AlN, allowing the Ti to bond strongly with the substrate [Ref. 73]. When a metal is then deposited on Ti, metallic bonds are formed between the film and the Ti inter-layer, giving rise to a film well bonded to the substrate. Accordingly, one would expect that the r.m.s. strain measured in the sample with the Ti inter-layer would be

larger than that in the sample without an inter-layer (AUALN3). However, as seen from Table 3, the sample with a Ti inter-layer had a r.m.s. strain much lower than the others. This result may be due to oxygen contamination of the Ti inter-layer during deposition, thereby preventing strong metallic bonding between the Au and AlN and resulting in low levels of plastic strain. Further chemical investigation of the interface regions are required to verify this hypothesis.

The Cr inter-layer sample that was metallized at a higher substrate temperature (AUALN8) shows a much lower degree of r.m.s. strain than for the Cr inter-layer sample (AUALN4) which was metallized at a lower substrate temperature. A possible explanation for this observation is that the inter-layer of the sample metallized at the higher substrate temperature could achieve a greater extent of stress relaxation (through increased dislocation movement) prior to the application of the Au film. This could result in less plastic stress being transferred to the Au film and less r.m.s. strain upon cooling.

Finally, the substrate treated with an oxide layer (AUALN7), showed a significant amount of r.m.s. strain. A possible explanation is that Au-O bonding occurred at the oxide-film interface when the high temperature Au metal first reached the oxide surface during metallization. Since it is known that oxygen diffuses extremely well into AlN, good bonding at both interfaces is possible, resulting in a large degree of plastic stress transfer to the Au film and high r.m.s. strain. This hypothesis would also require further chemical analysis.

The average particle size obtained from the Warren-Averbach analysis is a function of dislocation spacing, and the degree stacking faults and twinning. If the degree of stacking faults and twinning are the same for all the samples, then the particle sizes obtained in this study are indicative of the subgrain size of Au film. Obtaining stacking fault and twinning probabilities from X-ray diffraction, through the measurement of peak shifts relative to a

strain free standard of sufficient particle size, is possible [Ref. 74], and further studies using these methods would provide more information on the microstructure of the Au films produced.

3. Uncertainty

The APD 1700 software used to perform the Warren-Averbach analysis performs uncertainty estimates as well. Table 4 lists the uncertainties of both r.m.s. strain and particle size for each method used. It should be noted that the uncertainties listed apply to the computational methods used in the Warren-Averbach analysis phase of the APD 1700 program only, and do not represent the combined uncertainties of the metallization process or from the XRD measurements.

TABLE 4. UNCERTAINTY SUMMARY

SAMPLE	COSINE	METHOD	MODULUS	METHOD
	R.M.S. STRAIN %	PARTICLE SIZE %	R.M.S. STRAIN %	PARTICLE SIZE %
AUALN1	3.0	4.2	3.0	3.9
AUALN2	19.2	14.7	2.96	3.01
AUALN3	30.8	15.6	23.1	14.5
AUALN3	27.6	21.1	19.4	14.5
AUALN5	4.0	3.0	4.4	4.0
AUALN6	24.5	18.0	24.7	17.6
AUALN7	34.1	15.5	33.6	15.0
AUALN8	40.0	24.6	13.7	8.16
AAU1	17.9	18.2	18.7	17.8

V. CONCLUSIONS

The r.m.s. strain value increased as the surface roughness of the substrates was increased indicating a higher degree of plastic deformation for roughened substrates. It is suspected that a higher surface roughness improves mechanical interlocking between the film and the substrate which improves adhesion.

A lower metallization pressure resulted in a much higher value for r.m.s. strain, which indicates better adhesion is possible by improving vacuum during deposition. Less contamination of the substrate surface is a possible reason for this observation. Additionally, deposition pressure may effect the epitaxial growth of the film crystals which may be related to film adhesion.

The presence of an oxide layer was seen to raise the r.m.s. strain values significantly, indicating the possibility of metal-O bonding between the Au and the Alumina layer. Although improved adhesion is indicated with the presence of an oxide layer, the thermal conductivity of the $\text{AlN} / \text{Al}_2\text{O}_3 / \text{Au}$ system is most likely lower than the AlN / Au system due to oxygen diffusion into the AlN.

Measurable r.m.s. strains for metallizations using inter-layers indicated that the inter-layer does not act as a compliant layer. Additionally, the inter-layer is not likely to be acting as a separate entity since the ΔCTE between the inter-layer and the Au film does not account for the relative amounts of r.m.s. strain observed for the Cr and Ti inter-layer samples. It is believed that inter-layers act as surface modifiers that change the bonding characteristics of the interface in some way. A high r.m.s. strain value was observed using a Cr inter-layer, indicating it improves adhesion compared to a system with no inter-layer.

A Ti inter-layer was seen to produce a small r.m.s. strain value indicating less adhesion, possibly due to contamination of the Ti by oxygen diffusion during deposition.

VI. RECOMMENDATIONS

The following recommendations are given for further study of metallized AlN substrates:

- More Au thin films deposited on AlN substrates using the same substrate preparation parameters and metallizing conditions should be performed to improve the statistical reliability of these results.
- Careful analysis of the stacking fault and twinning probabilities from the X-ray data, and the extraction of real crystallite sizes should be used to supplement the r.m.s. strain data.
- TEM studies of the prepared films would be extremely useful in determining the amount of stacking and twin faults which could be used to verify the effective particle size results obtained in this study.
- The films prepared should be checked for adhesive strength by scratch or peel testing to allow the r.m.s. strain values obtained in this study to be directly correlated to adhesive strength. If a direct correlation indeed exists, then the r.m.s. strain values could be used directly to predict thin film performance without the need for destructive testing.
- Post-metallization heat treatments may hold promise in reducing residual stress levels, through dislocation movement, as well as allowing metal diffusion between the substrate, interlayer and film. Metal-to-metal bonding may also be improved at elevated metallization temperatures by increased diffusion. A systematic study of substrate metallization temperature and post-metallization heat treatments is therefore warranted.

LIST OF REFERENCES

1. Hanneman, R., Fox, L. R. and Mahalingham, M., "Thermal Design for Microelectronic Components", *Advances in Cooling Techniques for Computers*, Aung, W., ed., Hemisphere Pub. Corp., p.247, 1991.
2. Iwase, N., Anzai, K. and Shinozaki, K., "Aluminum Nitride Substrates Having High Thermal Conductivity", *Solid State Technol.*, Vol. 29, p.136, 1986.
3. Ref. 2., p.135.
4. Marchant, D. D., and Nemeck, T. E., "Aluminum Nitride: Preparation, Processing and Properties", *Proceedings of the International Symposium on Ceramic Substrates, 1987, Denver, Co.*, Yan, M. F., ed., p. 19, The American Ceramic Society, 1987.
5. Noyan, I. C. and Cohen, J. B., *Residual Stress, Measurement by Diffraction and Interpretation*, pp. 242-243., Springer-Verlag, 1987.
6. Warren, B. E., *Progress in Metal Physics*, Pergamon, Vol. 8, p.147, 1959.
7. Ref. 4., pp.29-32.
8. Ref. 4., p.29.
9. Ref. 4., pp. 29-20.
10. Sheppard, L. M., "Aluminum Nitride: A Versatile but Challenging Material", *Cer. Bull.*, Vol. 69, No. 11, p. 1802, 1990.
11. Ref. 10., p. 1802.
12. Ref. 4., p. 20.
13. Ref. 10., p. 1803.
14. Kuramoto, N., Taniguchi, H. and Aso. I., "Sintering and Properties of High Purity AlN Ceramics", *Proceedings of the International Symposium on Ceramic Substrates, 1987, Denver, Co.*, Yan, M. F., ed., p. 110, The American Ceramic Society, 1987.
15. Ref. 10., pp. 1803-1806.

16. Ref. 10., p. 1805.
17. Ref. 14., p. 107.
18. Ref. 10., p. 1805.
19. Weisenbach, L., Ikeda, J. A. S. and Chiang, Y. M., "Distribution and Sintering Aids in Aluminum Nitrides with High Thermal Conductivity.", *Proceedings of the International Symposium on Ceramic Substrates, 1987, Denver, Co.*, Yan, M. F., ed., The American Ceramic Society, p.107, 1987.
20. Ref. 3., p. 135.
21. Ref. 17., p. 133.
22. Westwood A. D. and Notis, M. R., "Electronic Packaging Materials Science III", Jaccodine R., Jackson, K. A. and Sundahl, R. C., eds., MRS, p. 331, 1988.
23. Ref. 11., p. 1810.
24. Westwood, A. D. and Notis, M. R., "Thermal Conductivity and Considerations for AlN Interfaces", *Ceram. Trans.*, Vol. 15, 1990, p.365.
25. Norton, M. G., "Thermodynamic Considerations in the Thick-Film metallization of Aluminum Nitride Substrates.", *J. Mater. Sci. Lett.*, Vol. 9, pp. 91-93, 1990.
26. Hitch, T. T., "Adhesion, Phase Morphology, and Bondability of Reactively-Bonded and Frit-Bonded Gold and Silver-Thick Film Conductors", *J. Electron. Mater* Vol. 3, pp. 553-575, 1974.
27. Zdanewski, W. A. and Houser, C. A., "Stereographic Fractography of Crack Propagation in a Ti - B₂ - AlN Composite", *J. Am. Ceram. Soc.*, Vol. 72, p. 2084, 1989.
28. Kurihara, Y., Takahashi, S., Yamada, K. and Endoh, T., "Ag-Pd Thick Film Conductor for AlN Ceramics", *IEEE CHMT*, Vol. 13, p. 306, 1989.
29. Ref. 10., p. 1809.
30. Ref. 10., pp. 1809-1810.
31. Miyashiro, F. and others, "High Thermal Conductivity Aluminum Nitride Ceramic Substrates and Packages", *IEEE CHMT*, Vol. 13, p. 319, 1990.

32. Ref. 31., p. 313.
33. Iwase, N., Anzai, K., Shinozaki, K., Hirao, O., Than, T. D. and Sugiura, Y., "Thick Film and Direct Bond Copper Forming Technologies for Aluminum Nitride Substrate", *IEEE CHMT*, Vol. 8, p. 253, 1985.
34. Dutta, I. and Mitra, S., "Oxidation of Sintered Aluminum Nitride at Near-Ambient Temperatures", *J. Am. Ceram. Soc.*, Vol. 11, p. 3149, 1992.
35. Ohuchi, F. S. and Kohyama, M., "Electronic Structure and Chemical Reactions at Metal/Alumina and Metal/Aluminum Nitride Interfaces", *J. Am. Ceram. Soc.*, Vol. 74, p. 1163, 1991.
36. Westwood, A. D. and Notis, M. R. "Advances in Ceramics", Vol. 26, *Ceramic Substrates and Packages*, Yan, M. F., ed., Am. Cer. Soc., p. 171, 1989.
37. Carim, A. H., "Identification and Characterization of $(\text{Ti, Cu, Al})_6\text{N}$, a New η Nitride Phase", *J. Mater. Res.*, Vol. 4, p. 1456, 1989.
38. Beyers, R., Sinclair, R. and Thomas, M. E., "Phase Equilibria in Thin-Film Metallizations", *J. Vac. Sci. Technol.*, Vol. B2, p. 781, 1984.
39. Gangulee, A., "The Structure of Electroplated and Vapor-Deposited Copper Films", *J. App. Phys.*, Vol. 43, p. 867, 1972.
40. Smithells, C. J., ed., *Metals Reference Book*, Butterworths, p. 123, 1976.
41. Schuster, J. C. and Nowotny, H., "Phase Relationships in the Ternary Systems (V, Cr, Mo, W, Mn, Re)-Al-N", *J. Mater. Sci.*, Vol. 20, p. 2787, 1985.
42. McDowell, C. B. and Pilkington, T. C., "X-Ray diffraction Methods for Determining Strain Distributions in Thin Metallic Films with applications to Gold Films", *J. App. Phys.*, Vol. 42, p. 2958, 1971.
43. Chopra, K. I., *Thin Film Phenomena*, p. 228, McGraw-Hill Book Co., 1969.
44. Ref. 43., p. 227.
45. Warren, B. E., *X-Ray Diffraction*, Chapt. 9, Addison-Wesley, pp. 264-275, 1971.
46. Klug, H. P. and Alexander, L. E., *X-Ray Diffraction Procedures*, Chapt. 9, John Wiley and Sons, 1974.

47. Ref., 45., p.264.
48. Culity, B. D., *Elements of X-Ray Diffraction*, pp. 103-105, Addison-Wesley Publishing Co., Inc., 1978.
49. Ref.45., pp. 264-275.
50. Ref. 46., p. 635.
51. Ref. 46., p. 643.
52. Ref. 48., p. 102.
53. Ref. 48., p.286.
54. Ref. 46., pp. 643-645.
55. Ref. 46., p.644.
56. Ref. 46., p.645.
57. Ref. 46., p. 650.
58. Ref. 5., pp. 242-243.
59. Delhez, R., de Keijser, Th. H. and Mittemeijer, E. J., "Determination of Crystallite size and Lattice Distortions through X-Ray Diffraction Line Profile Analysis; Recipes, Methods and Comments", *Fresenius Zeitschr. Anal. Chem.*, Vol., 312, pp. 7-8., 1982.
60. Ref. 59., pp. 1-16.
61. Ref. 46., p. 651.
62. Ref. 46., p. 654.
63. Ref. 59., p. 1-16.
64. Ref. 58., pp. 117-163.
65. Ref. 46., p.643.
66. Film Thickness Monitor No. 18980 Instruction Sheet, Ernest F. Fillam Inc., p. 2., 1992.

67. Jones, S. and Scott, W. D., "Low Temperature Oxidation of Dense Aluminum Nitride", *Ad. Ceram.*, Vol. 26, p. 152, 1989.
68. APD1700: Software for Automatic Powder Diffraction, N. V. Philips Gloeilampen-Fabrieken, Eindhoven, Holland, 1989.
69. d'Heurle, F. M., Berenbaum, L. and Rosenberg, R., "On the Structure of Aluminum Films", *Trans. Met. Soc. AIME*, pp. 502-505, 1968.
70. Christou, A. and Day, H., "Structure and Thermal Stability of Sputtered Au-Ta Films", *J. Appl. Phys.*, p. 3386, 1973.
71. Wagner, C. N. J., *Local Atomic Arrangements Studied by X-Ray Diffraction*, Cohen, J. B. and Hillard, J. E., eds., p. 291, Gordon and Breach, 1966.
72. Fox, A. G. and Cannon, R. M., "X-Ray Diffraction and TEM Studies of the Delamination of Copper Thin Films From Glass and Silica Substrates", *Mat. Res. Soc. Symp. Proc.*, Vol. 167, p. 329, 1990.
73. Ref. 37., p. 1456.
74. Ref. 45., pp. 288-298.

INITIAL DISTRIBUTION LIST

1. Defense Technical Information Center 2
Cameron Station
Alexandria, VA 22304-6145
2. Library, Code 52 2
Naval Postgraduate School
Monterey, CA 93943-5002
3. Naval Engineering Circular Office, Code 34 1
Naval Postgraduate School
Monterey, CA 93943-4004
4. Prof. I. Dutta, Code ME/DU 1
Department of Mechanical Engineering
Naval Postgraduate School
Monterey, CA 92943-5100
5. Prof. A. J. Healy, Code ME/HY 1
Chairman
Department of Mechanical Engineering
Naval Postgraduate School
Monterey, CA 93943-5100
6. LCDR Clifford B. Munns 1
800 W. Franklin St.
Monterey, CA 93940
7. Mr. Pat Sullivan 1
NCCOSC-RDT&E Div.
Code 551
271 Catalina Blvd.
San Diego, CA 92110

DUDLEY KNOX LIBRARY
NAVAL POSTGRADUATE SCHOOL
MONTEREY CA 93943-7100

GAYLORD S

DUDLEY KNOX LIBRARY



3 2768 00308495 5